J. Fluid Mech. (2022), *vol*. 951, A24, doi:10.1017/jfm.2022.848

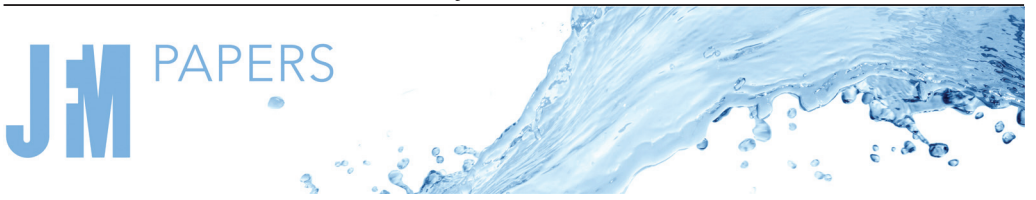

Asymptotic behaviour of rotating convection-driven dynamos in the plane layer geometry

Ming Yan[1] **and Michael A. Calkins**[1],†

[1]Department of Physics, University of Colorado, Boulder, CO 80309, USA

(Received 2 February 2022; revised 2 August 2022; accepted 28 September 2022)

Dynamos driven by rotating convection in the plane layer geometry are investigated numerically for a range of Ekman number (E), magnetic Prandtl number (Pm) and Rayleigh number (Ra). The primary purpose of the investigation is to compare results of the simulations with previously developed asymptotic theory that is applicable in the limit of rapid rotation. We find that all of the simulations are in the quasi-geostrophic regime in which the Coriolis and pressure gradient forces are approximately balanced at leading order, whereas all other forces, including the Lorentz force, act as perturbations. Agreement between simulation output and asymptotic scalings for the energetics, flow speeds, magnetic field amplitude and length scales is found. The transition from large-scale dynamos to small-scale dynamos is well described by the magnetic Reynolds number based on the small convective length scale, $\widetilde{Rm}$, with large-scale dynamos preferred when $\widetilde{Rm} \lesssim O(1)$. The magnitude of the large-scale magnetic field is observed to saturate and become approximately constant with increasing Rayleigh number. Energy spectra show that all length scales present in the flow field and the small-scale magnetic field are consistent with a scaling of $E^{1/3}$, even in the turbulent regime. For a fixed value of E, we find that the viscous dissipation length scale is approximately constant over a broad range of Ra; the ohmic dissipation length scale is approximately constant within the large-scale dynamo regime, but transitions to a $\widetilde{Rm}^{-1/2}$ scaling in the small-scale dynamo regime.

Key words: geodynamo, dynamo theory, Bénard convection

1. Introduction

The majority of solar system planets possess global-scale magnetic fields. These fields are believed to be generated by the convective motion of electrically conducting fluid within

† Email address for correspondence: michael.calkins@colorado.edu

the interior regions of the planets (Jones 2011). For example, the geomagnetic field of the Earth is thought to originate in the liquid metal outer core where buoyancy-driven flows continuously generate electric currents and associated magnetic field (Roberts & King 2013). One particular physical ingredient that is thought to be critical for sustaining large, or global, scale magnetic field is the Coriolis force (Parker 1955; Steenbeck, Krause & Rädler 1966). Although many previous investigations have shown the tendency for rotating convection to generate magnetic fields (beginning with Childress & Soward (1972) and Soward (1974)), it is still not completely understood how the various input parameters influence: (i) the characteristic length scales of the velocity and magnetic fields; (ii) the strength of the resulting magnetic fields; and (iii) the prevailing force balance that characterises the dynamics. However, the asymptotic theory developed by Calkins *et al.* (2015) provides predictions for these various properties. In this regard, we utilise direct numerical simulation (DNS) in the plane layer geometry to better understand how rotation, buoyancy and the relative influence of diffusion influence system behaviour. The simulation output is used to test various predictions from the asymptotic theory.

Natural dynamo systems such as the Earth's outer core are characterised by several small (or large) physical parameters (Jones 2011; Schubert & Soderlund 2011). In particular, the Ekman number, defined as $E = \nu/(\Omega H^2)$ (where ν is the kinematic viscosity, Ω is the rotation rate and H is the characteristic length scale), is very small; estimates suggest $E = O(10^{-15})$ in the core. The Rossby number, representing the ratio of inertia to the Coriolis force, is also small in the core; $Ro = U/(\Omega H) = O(10^{-6})$, where U is a characteristic speed. It is therefore of interest to understand how dynamos and rotating convection behave in the dual limit $(E, Ro) \to 0$.

Rotating convection has been investigated extensively in both the spherical and plane layer geometries, although computational restrictions prevent the use of realistic values of E. Significant progress has been made toward understanding the asymptotic theory of plane layer rotating convection; output from simulations of the fully nonlinear asymptotic model developed by Julien, Knobloch & Werne (1998) agrees well with the corresponding output from DNS (Stellmach *et al.* 2014; Plumley *et al.* 2016). In particular, this theory predicts that the flow will be geostrophically balanced to leading order – i.e. the Coriolis and pressure gradient forces should be approximately balanced and all other forces act as perturbations. Guzmán *et al.* (2021) explicitly computed the forces in plane layer rotating convection and have confirmed the dynamics is quasi-geostrophic (QG), provided the Rossby number remains small.

In comparison with the purely hydrodynamic rotating convection problem, the asymptotic behaviour of the dynamo problem is less well understood. In particular, accurately diagnosing the force balance remains an ongoing effort, and to complicate matters it appears that the force balance depends on the geometry, as well as the particular length scale on which the dynamics is analysed. Recent work in the spherical geometry points to a leading-order geostrophic balance on the small-scale motions (Yadav, Gastine & Christensen 2016; Aubert, Gastine & Fournier 2017; Schaeffer *et al.* 2017; Schwaiger, Gastine & Aubert 2021) and a semi-magnetostrophic force balance on the large scales (Aubert 2005; Calkins, Orvedahl & Featherstone 2021; Orvedahl, Featherstone & Calkins 2021). Here, the term 'semi-magnetostrophic' is used because the Lorentz force only enters the leading-order force balance in the zonal component of the large-scale momentum equation, and it is of smaller magnitude than the mean buoyancy force. For the small-scale dynamics in a spherical geometry, i.e. on the scale of the convection, the Lorentz force acts as a perturbation to the leading-order geostrophic balance (Yadav *et al.* 2016).

Another important parameter in natural dynamos is the magnetic Prandtl number, $Pm = \nu/\eta$, where η is the magnetic diffusivity. Estimates suggest values that range from

$Pm = O(10^{-3})$ in the interior regions of stars to as small as $Pm = O(10^{-6})$ in planetary interiors and the outer regions of stars (Ossendrijver 2003). Self-sustaining dynamos require sufficiently large flow speeds to counteract the effects of ohmic dissipation, as characterised by the magnetic Reynolds number, $Rm = UH/\eta$. The magnetic and hydrodynamic Reynolds numbers are related by $Rm = PmRe$, where $Re = UH/\nu = Ro/E$. Rotating dynamos typically require at least $Rm = O(10)$ to sustain dynamo action. Thus, for $Pm = O(10^{-6})$, Reynolds numbers in excess of $Re = O(10^7)$ would be required to generate self-sustaining magnetic fields. Such values of Re are well beyond the reach of current DNS and studies therefore must use unrealistically large values of Pm – typically $Pm = O(1)$. Recent state-of-the-art simulations in a spherical geometry have used values as small as $Pm = 0.05$ (Sheyko *et al.* 2018), though such simulations require enormous computational resources and therefore parameters cannot be varied systematically. The disparity in parameter values between DNS and natural dynamos leads to reasonable suspicion as to how the dynamics of these two systems relate to one another.

Dynamos are often distinguished by the typical length scale of the magnetic field (e.g. Tobias 2021). Large-scale dynamos have a component of the magnetic field that varies on a global length scale. In contrast, small-scale dynamos have a negligible large-scale component and are instead dominated by length scales comparable to that of the velocity field. Using weakly nonlinear asymptotic theory, Childress & Soward (1972) and Soward (1974) showed that rapidly rotating convection in the plane layer geometry can readily drive large-scale dynamo action near the onset of convection. In this geometry, the large-scale magnetic field is often defined as the horizontally averaged component of the field, which is required to be purely horizontal due to the solenoidal constraint on the magnetic field. Using the methods of Sprague *et al.* (2006), Calkins *et al.* (2015) developed a fully nonlinear extension of the Childress–Soward dynamo model – this extended model suggests that large-scale dynamo action is achievable for arbitrarily large forcing, so long as the convection remains geostrophically balanced. This model also predicts that the large-scale magnetic field remains energetically dominant relative to the small-scale magnetic field provided the magnetic Reynolds number based on the small, horizontal convective length scale is less than unity (Calkins, Julien & Tobias 2017; Calkins 2018) – this prediction is supported by recent numerical simulations (Yan & Calkins 2022). Other aspects of this asymptotic theory, including the scaling behaviour of the various physical quantities and the associated force balance remain untested.

Previous DNS investigations of dynamos in the plane layer geometry have confirmed that large-scale dynamo action is achievable, provided that the convection is rotationally constrained and Rm is not too large (e.g. Jones & Roberts 2000; Stellmach & Hansen 2004; Käpylä, Korpi & Brandenburg 2009; Guervilly, Hughes & Jones 2017). As the buoyancy forcing is increased at a fixed value of E, the dynamo transitions from a large-scale dynamo to a small-scale dynamo (e.g. Tilgner 2012), although the influence of rotation must be sufficiently strong to observe this transition (e.g. Cattaneo & Hughes 2006; Favier & Bushby 2013). A similar relationship between the effects of rotation, buoyancy force and magnetic field morphology is well known in spherical geometries (Kutzner & Christensen 2002; Christensen & Aubert 2006; Soderlund, King & Aurnou 2012). For certain values of Pm there exists an intermediate regime in the plane layer geometry in which no dynamo is observed (Tilgner 2012; Guervilly *et al.* 2017). Moreover, Guervilly *et al.* (2017) found that significant large-scale magnetic energy could be generated for strongly supercritical flows if large-scale vortices (LSVs) are present. Such LSVs are the consequence of an inverse kinetic energy cascade in which kinetic energy is transferred from small-scale convective motions to domain-scale flows (Julien *et al.* 2012; Favier, Silvers & Proctor

2014; Guervilly, Hughes & Jones 2014; Rubio *et al.* 2014). In a Cartesian domain of square cross-section the vortices are depth invariant, and for sufficiently small Rossby numbers are dipolar in structure (Stellmach *et al.* 2014), but become predominantly cyclonic at larger Rossby numbers (Favier *et al.* 2014; Guervilly *et al.* 2014). Magnetic fields of sufficient magnitude can damp the vortices and prevent their formation (Guervilly *et al.* 2017; Bushby *et al.* 2018; Maffei *et al.* 2019).

In the present study we investigate convection-driven dynamos in the rapidly rotating regime. One of our primary goals is to understand the asymptotic behaviour of the resulting dynamos, including heat transfer, flow speed, magnetic field strength, length scales and force balances. This analysis has not been performed previously, and we find that the simulations are consistent with much of the theory of Calkins *et al.* (2015), including the asymptotic scaling behaviour and the prediction that large-scale dynamo action is achieved for arbitrarily large forcing as long as $E \to 0$ and $Pm \to 0$. In § 2 we present the non-dimensional equations, physical parameters and the numerical methods employed. The asymptotic theory of rapidly rotating dynamos in the plane layer geometry is briefly summarised in § 3, results are discussed in § 4 and a discussion is given in § 5.

2. Governing equations and methods

We consider an electrically conducting Boussinesq fluid layer of depth H contained between two plane parallel boundaries. The system is heated from the bottom and cooled from the top, with the temperature difference $\Delta T = T_{bot} - T_{top} > 0$, where T_{bot} and T_{top} are the temperatures at the bottom and top boundaries, respectively. A constant gravitational acceleration is used and given by $\boldsymbol{g} = -g\hat{\boldsymbol{z}}$, where $\hat{\boldsymbol{z}}$ points from the bottom boundary to the top boundary. The rotation of the system is characterised by a constant rotation rate, $\boldsymbol{\Omega} = \Omega\hat{\boldsymbol{z}}$. The fluid has density ρ, kinematic viscosity ν, thermal diffusivity κ, thermal expansion coefficient γ, magnetic diffusivity η and vacuum permeability μ_0. The governing equations are non-dimensionalised with depth H, time scale $2\Omega^{-1}$ and magnetic field scale $\mathcal{B} = 2\Omega H\sqrt{\rho\mu_0}$, and are given by

$$D_t\boldsymbol{u} + \hat{\boldsymbol{z}} \times \boldsymbol{u} = -\boldsymbol{\nabla} p + (\boldsymbol{\nabla} \times \boldsymbol{B}) \times \boldsymbol{B} + \frac{E^2 Ra}{Pr}\theta\hat{\boldsymbol{z}} + E\nabla^2\boldsymbol{u}, \tag{2.1}$$

$$D_t\theta = \frac{E}{Pr}\nabla^2\theta, \tag{2.2}$$

$$\partial_t\boldsymbol{B} = \boldsymbol{\nabla} \times (\boldsymbol{u} \times \boldsymbol{B}) + \frac{E}{Pm}\nabla^2\boldsymbol{B}, \tag{2.3}$$

$$\boldsymbol{\nabla} \cdot \boldsymbol{u} = 0, \tag{2.4}$$

$$\boldsymbol{\nabla} \cdot \boldsymbol{B} = 0, \tag{2.5}$$

where the material derivative is denoted by $D_t(\,\cdot\,) = \partial_t(\,\cdot\,) + \boldsymbol{u} \cdot \boldsymbol{\nabla}(\,\cdot\,)$. We denote the velocity field as $\boldsymbol{u} = (u, v, w)$, the magnetic field as $\boldsymbol{B} = (B_x, B_y, B_z)$, the temperature as θ, the pressure as p and the Cartesian coordinate system as (x, y, z).

The non-dimensional control parameters are the Rayleigh number (Ra), the thermal Prandtl number (Pr), the magnetic Prandtl number (Pm) and the Ekman number (E), defined as

$$Ra = \frac{g\gamma\Delta T H^3}{\nu\kappa}, \quad Pr = \frac{\nu}{\kappa}, \quad Pm = \frac{\nu}{\eta}, \quad E = \frac{\nu}{2\Omega H^2}. \tag{2.6a–d}$$

For simplicity we fix the thermal Prandtl number at $Pr = 1$ for all simulations.

In the limit of asymptotically small Ekman number the dynamics depends not on Ra and E independently, but on the combination (e.g. see Julien *et al.* 2012)

$$\widetilde{Ra} \equiv E^{4/3} Ra, \tag{2.7}$$

which is consistent with the asymptotic scaling for the critical Rayleigh number, i.e. $Ra_c = O(E^{-4/3})$ (Chandrasekhar 1961). This asymptotically rescaled Rayleigh number will be used throughout.

We apply impenetrable and stress-free velocity boundary conditions at the top and bottom boundaries,

$$w = \frac{\partial u}{\partial z} = \frac{\partial v}{\partial z} = 0 \quad \text{at } z = 0, 1. \tag{2.8}$$

We use vertical magnetic field boundary conditions such that

$$B_x = B_y = \frac{\partial B_z}{\partial z} = 0 \quad \text{at } z = 0, 1. \tag{2.9}$$

The thermal boundary conditions are isothermal,

$$\theta = 1 \quad \text{at } z = 0, \quad \text{and} \quad \theta = 0 \quad \text{at } z = 1. \tag{2.10a,b}$$

Periodic boundary conditions are used in the horizontal directions. For a detailed discussion on the influence of thermal, mechanical and electromagnetic boundary conditions on dynamos we refer the reader to Kolhey, Stellmach & Heyner (2022). In addition, Roberts & Zhang (2000) have shown that the choice of electromagnetic boundary conditions can have a strong influence on the linear properties of magnetoconvection.

2.1. *Diagnostic quantities*

The volumetric and time-averaged kinetic energy density E_{kin} and magnetic energy density E_{mag} are calculated as

$$E_{kin} \equiv \frac{1}{2E^2} \langle \boldsymbol{u}^2 \rangle, \tag{2.11}$$

and

$$E_{mag} \equiv \frac{1}{2E^2} \langle \boldsymbol{B}^2 \rangle, \tag{2.12}$$

where angled brackets, $\langle \cdot \rangle$, denote a volumetric and time average.

We decompose the magnetic field into horizontally averaged (mean) and fluctuating components according to $\boldsymbol{B}(x, y, z, t) = \bar{\boldsymbol{B}}(z, t) + \boldsymbol{B}'(x, y, z, t)$, where the overline $\overline{(\cdot)}$ denotes a horizontal average. The corresponding mean and fluctuating magnetic energy are then defined by, respectively,

$$\bar{E}_{mag} = \frac{1}{2E^2} \int_0^1 \bar{\boldsymbol{B}}^2 \, \mathrm{d}z, \tag{2.13}$$

and

$$E'_{mag} = E_{mag} - \bar{E}_{mag}. \tag{2.14}$$

Note that, while this particular definition of the mean magnetic field is simple, it has the disadvantage that any motion characterised by a horizontal wavenumber greater than zero is defined as small scale.

The Reynolds number Re is used to quantify the non-dimensional flow speed and is computed by

$$Re = \sqrt{2E_{kin}}. \tag{2.15}$$

Decomposing the temperature into mean and fluctuating components, $\theta(x, y, z, t) = \bar{\theta}(z, t) + \theta'(x, y, z, t)$, we define the Nusselt number Nu according to

$$Nu = -\left.\frac{\partial \bar{\bar{\theta}}}{\partial z}\right|_{z=0}, \tag{2.16}$$

where the additional overline indicates the quantity is also averaged in time. The exact relationship between the Nusselt number and the two sources of dissipation can be derived from the governing equations to give (e.g. Yan, Tobias & Calkins 2021)

$$\frac{Ra}{Pr^2}(Nu - 1) = \varepsilon_u + \varepsilon_B. \tag{2.17}$$

The viscous dissipation and ohmic dissipation are defined by, respectively,

$$\varepsilon_u = \frac{1}{E^2}\langle \boldsymbol{\zeta}^2 \rangle, \quad \varepsilon_B = \frac{1}{PmE^2}\langle \boldsymbol{J}^2 \rangle, \tag{2.18a,b}$$

where the vorticity and current density vectors are denoted by $\boldsymbol{\zeta} = \boldsymbol{\nabla} \times \boldsymbol{u}$ and $\boldsymbol{J} = \boldsymbol{\nabla} \times \boldsymbol{B}$, respectively.

2.2. *Numerical methods*

The velocity and magnetic field vectors are represented in terms of poloidal and toroidal scalars such that the solenoidal conditions are satisfied exactly (e.g. Jones & Roberts 2000; Marti, Calkins & Julien 2016). The resulting variables are expanded in Fourier series in the horizontal dimensions and Chebyshev polynomials in the vertical dimension. The nonlinear terms are de-aliased with the standard 2/3-rule. The equations are discretised in time with a third-order implicit–explicit Runge–Kutta scheme (Spalart, Moser & Rogers 1991). The code has been used in previous investigations (e.g. Yan *et al.* 2019, 2021), and the dynamo model used for the present study has been benchmarked with the work of Stellmach & Hansen (2004).

An important non-dimensional parameter characterising the geometry is the aspect ratio Γ, defined as

$$\Gamma = \frac{L}{H}, \tag{2.19}$$

where L is the periodicity length in the horizontal direction. In the present work only domains of square cross-section are used. We scale the horizontal periodicity length with the (non-dimensional) critical horizontal wavelength, λ_c, so that

$$L = n\lambda_c H, \tag{2.20}$$

where n is the integer number of critical horizontal wavelengths. This normalisation for the horizontal dimensions is done to ensure that the most unstable wavelength is present near the onset of convection. Thus, for our simulations, the aspect ratio is given by

$$\Gamma = n\lambda_c. \tag{2.21}$$

All of the results presented use $n = 10$ since this value was found to be sufficient for observing convergence of the primary global diagnostic quantities. The critical wavelength

is determined from the relationship (Chandrasekhar 1961)

$$2k_c^6 + 3k_c^4\pi^2 - \pi^6 - \pi^2 E^{-2} = 0, \tag{2.22}$$

where $k_c = 2\pi/\lambda_c$ is the critical horizontal wavenumber. The above relationship can be derived from the governing equations upon linearising about a state of rest.

3. Asymptotic theory

One of the main purposes of the present investigation is to shed light on the behaviour of rotating convection-driven dynamos in the asymptotic limit $E \to 0$, since this limit is relevant for natural systems. Since the asymptotic scalings will be used in the analysis of the results, we briefly summarise the theory here. This approach is general and can be used to analyse the asymptotic behaviour of DNS output, although the observed scalings will be dependent on the particular non-dimensionalisation that is employed.

If both the Rossby number and the Ekman number are small, the leading-order force balance will be geostrophic and the resulting QG dynamics is the result of small perturbations away from this balance. As previously mentioned, QG dynamo theory can be considered a fully nonlinear generalisation of the weakly nonlinear theory developed by Childress & Soward (1972), and studied in detail by Soward (1974). We note that the hydrodynamic QG theory shows excellent agreement with DNS results (Stellmach *et al.* 2014; Plumley *et al.* 2016); in the present work we demonstrate that the corresponding QG dynamo theory also shows excellent agreement with DNS.

The aim of QG theory is to understand the dynamics of rapidly rotating convection-driven dynamos based on a perturbation expansion. The relevant small parameter is the Rossby number based on the small-scale horizontal convective length scale, ℓ,

$$\epsilon \equiv \frac{U}{2\Omega\ell}. \tag{3.1}$$

We recall that U is the characteristic dimensional scale for the velocity field. Here, we scale the velocity in small-scale viscous diffusion units, $U = \nu/\ell$, such that

$$\epsilon = \frac{\nu}{2\Omega\ell^2} = \left(\frac{\nu}{2\Omega H^2}\right)\left(\frac{H}{\ell}\right)^2. \tag{3.2}$$

Using $\ell = HE^{1/3}$ the above relationship becomes

$$\epsilon = E^{1/3}. \tag{3.3}$$

This scaling is the relevant distinguished limit relating the small-scale Rossby number and the large-scale Ekman number, and allows for a self-consistent set of asymptotically reduced equations (Julien *et al.* 1998; Calkins *et al.* 2015).

The large-scale Rossby number and the small-scale Rossby number are related via

$$Ro = \frac{U}{2\Omega H} = \frac{U}{2\Omega\ell}\frac{\ell}{H} = E^{2/3} = \epsilon^2. \tag{3.4}$$

This relationship is useful for scaling the various terms in the momentum equation, since our particular choice of non-dimensionalisation implies that flow speeds are in units of the

large-scale Rossby number. Thus, denoting the magnitude of the velocity as u, we have

$$u = O\left(\epsilon^2\right), \tag{3.5}$$

where we note that all three velocity components have the same asymptotic scaling behaviour. With this asymptotic scaling for the flow speed, and assuming that all horizontal derivatives are $O(\epsilon^{-1})$ and vertical derivatives are order one, i.e. $\partial_z = O(1)$, we can estimate the asymptotic size of various terms in the momentum equation and other quantities that will be useful for analysing the results of the numerical simulations.

The leading-order geostrophic force balance implies that the Coriolis force and the pressure gradient force are the largest terms in the momentum equation. The asymptotic size of the Coriolis force is then

$$|\hat{\boldsymbol{z}} \times \boldsymbol{u}| = O(\epsilon^2) = O(E^{2/3}). \tag{3.6}$$

With the exception of the leading-order pressure gradient force, all other terms are asymptotically smaller than the above scaling, although the relative size of these asymptotically subdominant terms is crucial for the resulting QG dynamics. The viscous force is of size

$$|E\nabla^2 \boldsymbol{u}| = O(\epsilon^3) = O(E). \tag{3.7}$$

The buoyancy force must be of the same asymptotic size as the viscous force; this requires that the temperature perturbation $\theta' = \theta - \bar{\theta} = O(\epsilon)$ such that

$$\left|\frac{RaE^2}{Pr}\theta'\right| = \frac{\widetilde{Ra}E^{2/3}}{Pr}\left|\theta'\right| = O(\epsilon^3) = O(E). \tag{3.8}$$

The asymptotic size of the nonlinear momentum advection term is then

$$|\boldsymbol{u} \cdot \nabla \boldsymbol{u}| = O(\epsilon^3) = O(E). \tag{3.9}$$

If we assume the Lorentz force is also of the same size as these asymptotically subdominant terms then we have

$$|\,(\nabla \times \boldsymbol{B}) \times \boldsymbol{B}| = O(\epsilon^3) = O(E) \quad \Rightarrow \quad B = O(\epsilon^2) = O(E^{2/3}), \tag{3.10}$$

where B is the magnitude of the magnetic field vector. Like the velocity field, the asymptotic scaling is the same for all three components of the magnetic field. To summarise, the Coriolis and pressure gradient forces are both of size $O(E^{2/3})$, and all other forces are smaller by a factor of $E^{1/3}$. We note that the magnitude of the mean magnetic field can become asymptotically larger than the magnitude of the fluctuating magnetic field, although this requires $RmE^{1/3} \ll 1$ (Calkins *et al.* 2015). Our estimate for the asymptotic size of the magnetic field given above assumes that $RmE^{1/3} = O(1)$.

With the above scalings we can provide asymptotic estimates for other quantities of interest. The viscous dissipation scales as

$$\varepsilon_u = \frac{1}{E^2}\langle(\nabla \times \boldsymbol{u})^2\rangle = O(\epsilon^{-4}) = O(E^{-4/3}). \tag{3.11}$$

Similarly, the ohmic dissipation scales as

$$\varepsilon_B = \frac{1}{PmE^2}\langle(\nabla \times \boldsymbol{B})^2\rangle = O(\epsilon^{-4}) = O(E^{-4/3}). \tag{3.12}$$

An alternative derivation of these scalings is to use (2.17) and to substitute $Ra = \epsilon^{-4}\widetilde{Ra}$ such that

$$\frac{\widetilde{Ra}}{Pr^2}\,(Nu - 1) = \epsilon^4\,(\varepsilon_u + \varepsilon_B)\,. \tag{3.13}$$

In order for Nu to be independent of the Ekman number, this requires $\epsilon^4\varepsilon_u = O(1)$ and $\epsilon^4\varepsilon_B = O(1)$, and therefore both forms of dissipation must scale as ϵ^{-4}.

The kinetic and magnetic energy scale as

$$E_{kin} = O\left(\frac{u^2}{E^2}\right) = O\left(\epsilon^{-2}\right) = O\left(E^{-2/3}\right), \tag{3.14}$$

and

$$E_{mag} = O\left(\frac{B^2}{E^2}\right) = O\left(\epsilon^{-2}\right) = O\left(E^{-2/3}\right). \tag{3.15}$$

We emphasise that the above asymptotic relationships only specify the dependence on the Ekman number. In general, the various quantities still depend on the reduced Rayleigh number.

4. Results

In the simulations we vary the Ekman number, the Rayleigh number and the magnetic Prandtl number. The thermal Prandtl number is fixed at $Pr = 1$ for all simulations – we refer the reader to Aurnou *et al.* (2018) and Vogt, Horn & Aurnou (2021) for detailed investigations on the influence of small values of Pr, as relevant to liquid metals and plasmas. The Ekman number is varied from $E = 10^{-8}$ to $E = 10^{-4}$. The Rayleigh number is varied from $1.3Ra_c$ up to $9Ra_c$. For simplicity we will often translate these supercritical values to reduced Rayleigh numbers $\widetilde{Ra}$; we reach up to $\widetilde{Ra} \approx 78$. The magnetic Prandtl number is varied less extensively, but we consider values of $Pm = (1, 0.3, 0.2, 0.1, 0.05)$. For $Pm = 1$ we consider Ekman numbers from $E = 10^{-4}$ down to $E = 10^{-6}$. Since smaller values of E allow us to reach smaller values of Pm, we consider $Pm < 1$ for $E \leqslant 10^{-6}$. Various input and output quantities, along with numerical parameters, are listed in Tables 1–4 of the Appendix.

4.1. *Dynamo and flow regimes*

The different dynamo regimes can be characterised by the fraction of the mean magnetic energy to the total magnetic energy, $\bar{E}_{mag}/E_{mag}$, as shown in figures 1(*a*) and 1(*b*), where this quantity is plotted as a function of $\widetilde{Ra}$ and the reduced magnetic Reynolds number, $\widetilde{Rm} = E^{1/3}Rm$, respectively. For the purpose of discussion we classify dynamos as large scale if $\bar{E}_{mag}/E_{mag} \geqslant 0.5$; dynamos with smaller values are then referred to as small-scale dynamos. For fixed values of E and Pm the mean energy fraction generally decreases with increasing $\widetilde{Ra}$. In general we find that smaller values of Pm allow for larger values of $\bar{E}_{mag}/E_{mag}$, with some cases approaching unity. As shown in panel (*a*), larger values of $\bar{E}_{mag}/E_{mag}$ exist over a larger range in $\widetilde{Ra}$ for decreasing values of Pm, indicating that magnetic diffusion plays an important role in the relative strength of the large-scale magnetic field (e.g. Yan & Calkins 2022). When the energy fraction is plotted as a function of $\widetilde{Rm}$ in panel (*b*), we find a collapse of the data. In agreement with the theory of Calkins *et al.* (2015), the mean magnetic energy is predicted to dominate when $\widetilde{Rm} \ll 1$. Although

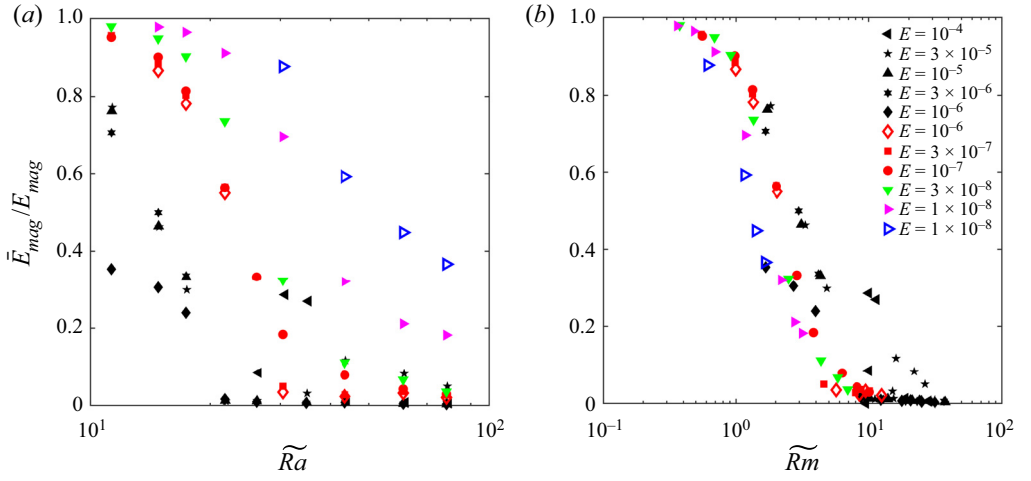

Figure 1. Overview of the dynamo regimes, as characterised by the fraction of the mean magnetic energy to the total magnetic energy, $\bar{E}_{mag}/E_{mag}$, in all simulations: (*a*) $\bar{E}_{mag}/E_{mag}$ vs reduced Rayleigh number, $\widetilde{Ra}$; (*b*) $\bar{E}_{mag}/E_{mag}$ vs reduced magnetic Reynolds number, $\widetilde{Rm}$. Symbol shape represents different values of the Ekman number (E) and colour represents different values of the magnetic (Pm): black indicates $Pm = 1$; red indicates $Pm = 0.3$; green indicates $Pm = 0.2$; magenta indicates $Pm = 0.1$; blue indicates $Pm = 0.05$.

the simulations do not reach very small values of $\widetilde{Rm}$, there is nevertheless an observed trend of increasing $\bar{E}_{mag}/E_{mag}$ as $\widetilde{Rm}$ is decreased.

Guervilly *et al.* (2017) have found that it is possible to generate large-scale dynamos with the aid of LSVs for $E = 5 \times 10^{-6}$, provided that the magnetic Reynolds number is within the range $100 \lesssim Rm \lesssim 550$ and $Pm < 1$; in terms of the small-scale magnetic Reynolds number this range becomes $1.7 \lesssim \widetilde{Rm} \lesssim 9.4$. Guervilly *et al.* (2017) do not list values of $\bar{E}_{mag}/E_{mag}$, although visual inspection of their magnetic energy spectra shows that they do not observe large-scale dynamos in which the large-scale magnetic field is energetically dominant relative to the small-scale magnetic field. This finding is consistent with figure 1(*b*) for comparable parameter values in which $\bar{E}_{mag}/E_{mag} \lesssim 0.5$. For hydrodynamic convection with $E \ll 1$ and $Pr = 1$, LSVs become energetically dominant (relative to the small-scale velocity field) for $\widetilde{Ra} \gtrsim 20$ (Maffei *et al.* 2021), so that they are certainly present in many of the simulations presented here. However, our data and the asymptotic theory (e.g. see Yan & Calkins 2022) indicate that large-scale dynamo action is more directly controlled by the small-scale magnetic Reynolds number. Moreover, kinematic investigations of QG convection suggest that LSVs do not appear to alter the onset of dynamo action (Calkins *et al.* 2016). Additional insight into the role that LSVs play in dynamo action could be made by performing a set of simulations in which the depth-averaged flow is set to zero at each timestep (e.g. Maffei *et al.* 2021).

The flow regimes observed in the present study are broadly consistent with the regimes identified in previous studies of non-magnetic rotating convection (e.g. Julien *et al.* 2012), though in the present study we do not attempt to characterise precisely the location (in parameter space) of possible transitions. The presence of a magnetic field can certainly influence the regimes, as discussed, for instance, by Guervilly *et al.* (2017) and Maffei *et al.* (2019). Given the broad range of parameter values used here, we simply highlight some of the main effects of varying parameters on the observed flow regimes.

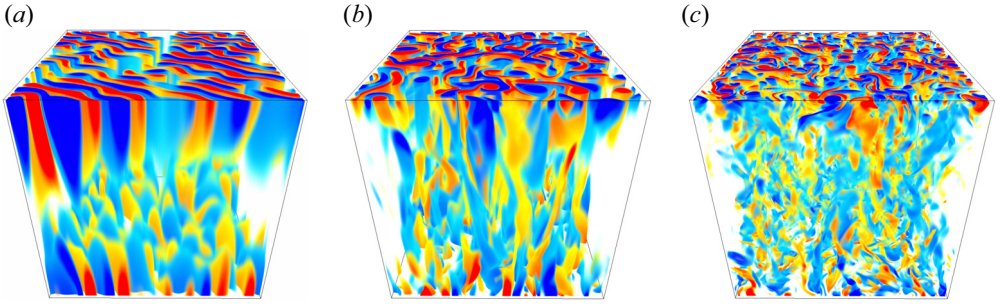

Figure 2. Volumetric renderings of the instantaneous vertical vorticity for $E = 10^{-8}$, $Pm = 0.1$ and increasing Rayleigh number from left to right: (*a*) $Ra = 1.7Ra_c$ ($\widetilde{Ra} \approx 15$); (*b*) $Ra = 3.5Ra_c$ ($\widetilde{Ra} \approx 30$); (*c*) $Ra = 9Ra_c$ ($\widetilde{Ra} \approx 78$). Red denotes positive (cyclonic) vorticity and blue denotes negative (anti-cyclonic) vorticity.

Figure 2 shows perspective views of the instantaneous vertical vorticity for three values of the Rayleigh number at the lowest Ekman number considered here, $E = 10^{-8}$, and $Pm = 0.1$. The corresponding mean magnetic energy fraction for panels (*a–c*) is, respectively, $\bar{E}_{mag}/E_{mag} \approx (0.98, 0.7, 0.18)$. Thus, cases shown in (*a*,*b*) are well within the large-scale dynamo regime. For relatively small reduced Rayleigh numbers ($\widetilde{Ra} \approx 15$) we find cellular structures, in the sense that the horizontal structure of the flow is relatively simple and dominated by the critical wavenumber. These cells become less coherent as $\widetilde{Ra}$ is increased, and geostrophic turbulence, as characterised by a leading-order geostrophic balance with a broad range of length scales that lack significant vertical coherence (e.g. Julien *et al.* 2012) is observed for sufficiently large ($\widetilde{Ra} \gtrsim 40$) Rayleigh number, as shown in figure 2(*c*). For the particular set of parameters shown in figure 2, we do not observe an obvious LSV at any value of $\widetilde{Ra}$, even for $\widetilde{Ra} \approx 78$ in which $\widetilde{Re} \approx 30$. As discussed later, cases with energetically dominant LSVs are characterised by horizontal kinetic energy spectra that show a peak at the smallest wavenumber, although these LSVs can become damped by the magnetic field (Guervilly *et al.* 2017; Maffei *et al.* 2019). Previous studies of hydrodynamic convection show that LSVs become energetically dominant when $\widetilde{Re} \gtrsim 6$ (Maffei *et al.* 2021), although this criterion is no longer valid when magnetic field is present.

A comparison of the flow morphology observed for different Ekman numbers is presented in figure 3, where top-down views of the vertical component of the vorticity are shown for $E = (10^{-4}, 10^{-6}, 10^{-8})$ (top to bottom in the figure) and $\widetilde{Ra} \approx 30$ (*a*,*c*,*e*) and $\widetilde{Ra} \approx 78$ (*b*,*d*,*f*). In terms of the dynamo regimes represented by these visualisations, only case (*e*) is within the large-scale dynamo regime, and all other cases are classified as small-scale dynamos. Whereas similar flow structures are observed for $E = 10^{-6}$ and $E = 10^{-8}$ when $\widetilde{Ra} \approx 30$ in which both positive (cyclonic, red) and negative (anti-cyclonic, blue) vorticity show similar structure, the case with $E = 10^{-4}$ and $\widetilde{Ra} \approx 30$ (figure 3*a*) shows significant asymmetry between cyclonic and anti-cyclonic vorticity. For this latter case we find that cyclonic structures occur in thin sheets that surround anti-cyclonic vortices. As the Rayleigh number is increased to $\widetilde{Ra} \approx 78$, figure 3(*b*) shows that the anti-cyclonic structures near the top boundary become weak and the cyclonic sheets are more distinct for $E = 10^{-4}$. We note that this particular case for $E = 10^{-4}$ and $\widetilde{Ra} \approx 78$ is in the small-scale dynamo regime in which the large-scale magnetic field represents less than 0.6 % of the total magnetic energy.

For $\widetilde{Ra} \approx 78$, we observe differences in the flow morphology between $E = 10^{-6}$ and $E = 10^{-8}$, as shown in figures 3(*d*) and 3(*f*). The case shown in panel (*d*) appears similar

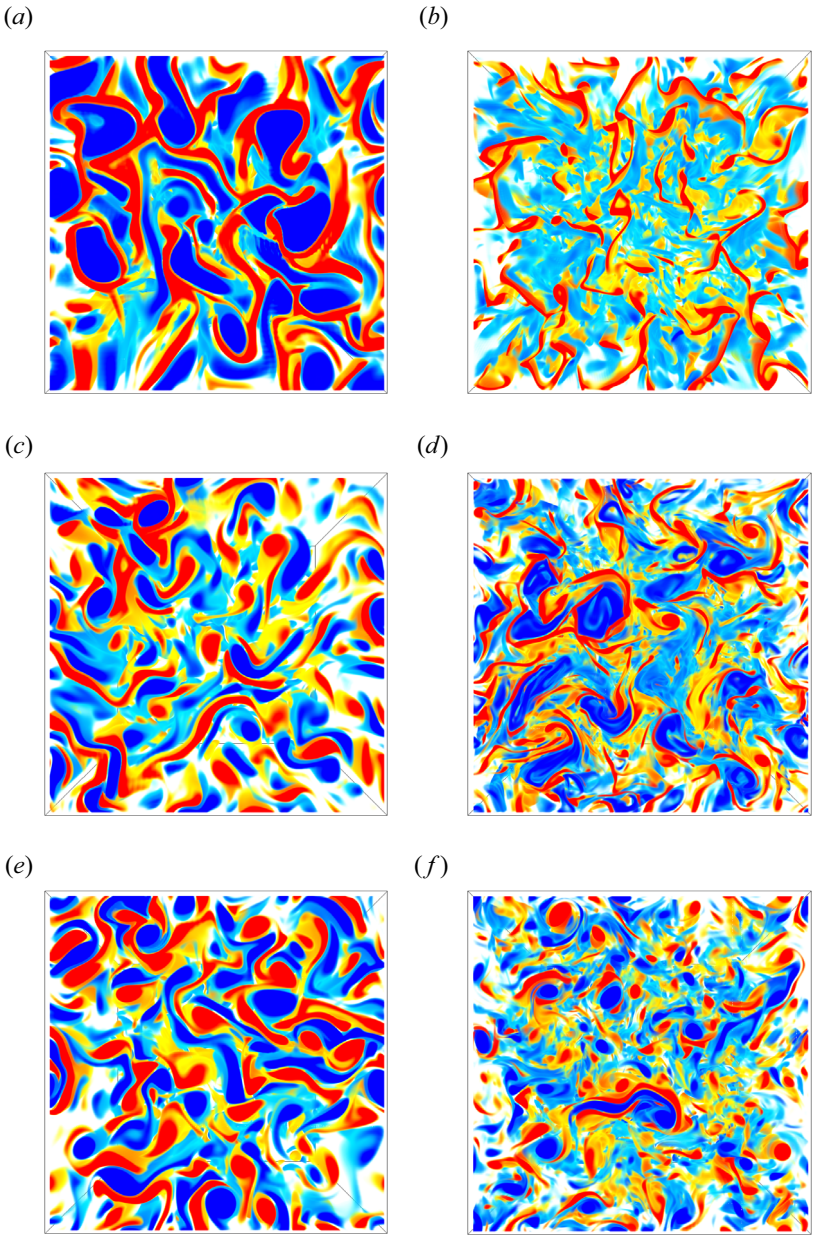

Figure 3. Top-down view of volumetric renderings of the instantaneous vertical vorticity for a range of Ekman and Rayleigh numbers. The Rayleigh number $\widetilde{Ra}$ increases from left to right and the Ekman number E decreases from top to bottom: (*a*) $E = 10^{-4}$, $Ra = 3.5Ra_c$ ($\widetilde{Ra} \approx 31$) and $Pm = 1$; (*b*) $E = 10^{-4}$, $Ra = 9Ra_c$ ($\widetilde{Ra} \approx 79$) and $Pm = 1$; (*c*) $E = 10^{-6}$, $Ra = 3Ra_c$ ($\widetilde{Ra} \approx 26$) and $Pm = 1$; (*d*) $E = 10^{-6}$, $Ra = 9Ra_c$ ($\widetilde{Ra} \approx 78$) and $Pm = 1$; (*e*) $E = 10^{-8}$, $Ra = 3.5Ra_c$ ($\widetilde{Ra} \approx 30$) and $Pm = 0.1$; (*f*) $E = 10^{-8}$, $Ra = 9Ra_c$ ($\widetilde{Ra} \approx 78$) and $Pm = 0.1$.

in structure to panel (*a*); this similarity hints at a finite Rossby number effect, suggesting that such structure might also be observed for $E = 10^{-8}$ if the Rayleigh number could be extended to larger values beyond those accessible in the present study. In contrast, panel (*f*) shows a more symmetric state. Whereas the case shown in (*d*) is within the small-scale

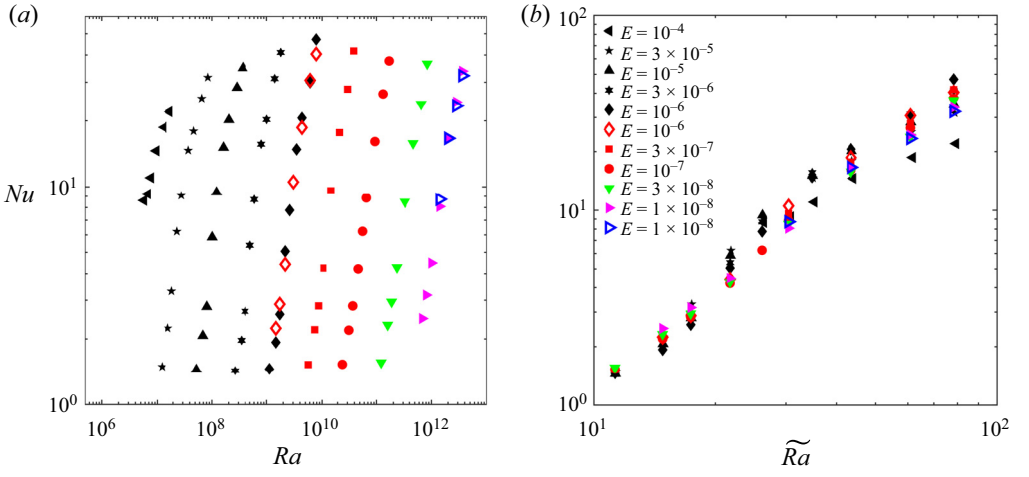

Figure 4. Heat transfer data: (*a*) Nusselt number, *Nu*, vs Rayleigh number, *Ra*; (*b*) *Nu* vs reduced Rayleigh number, $\widetilde{Ra} = E^{4/3}Ra$. Symbol shape represents different values of the Ekman number (E) and colour represents different values of the magnetic (Pm): black indicates $Pm = 1$; red indicates $Pm = 0.3$; green indicates $Pm = 0.2$; magenta indicates $Pm = 0.1$; blue indicates $Pm = 0.05$.

dynamo regime, the large-scale magnetic field for the case shown in (*f*) remains significant (≈20 % of the total magnetic energy). We note that the asymptotic scalings presented in the previous section are strictly valid only when the Rossby number remains small and symmetry is preserved.

4.2. *Heat transfer and dissipation*

The Nusselt number is shown as a function of the Rayleigh number in figure 4(*a*) for all cases; it is shown as a function of $\widetilde{Ra}$ in panel (*b*). As with the flow regimes discussed in the previous subsection, we observe heat transport behaviour that is similar to hydrodynamic rotating convection (e.g. Aurnou *et al.* 2015). While there is some variation in the data for different values of E, all of the cases show broadly similar behaviour when plotted as a function of the reduced Rayleigh number, indicating the simulations are in an asymptotic dynamical regime. The Nusselt number shows a characteristic 's'-shaped dependence on $\widetilde{Ra}$ that is well known in the literature for rotating convection (e.g. Cheng *et al.* 2015); for the smallest values of $\widetilde{Ra}$, *Nu* rises steeply at first, then slows at larger values of $\widetilde{Ra}$ as the Rossby number increases. For a fixed value of $\widetilde{Ra}$, the variation in *Nu* may be due to the differences in observed dynamo behaviour. For instance, whereas some of the cases shown have significant mean magnetic fields, other cases are within the small-scale dynamo regime and therefore generate mean magnetic fields with negligible amplitude.

Figures 5(*a*) and 5(*b*) show the asymptotically rescaled viscous dissipation $\varepsilon_u E^{4/3}$ and the asymptotically rescaled ohmic dissipation $\varepsilon_B E^{4/3}$ plotted as a function of the reduced Rayleigh number $\widetilde{Ra}$. Consistent with the energy relationship (2.17), both forms of the dissipation show behaviour that is consistent with the Nusselt number. Sudden changes in ε_u, and discontinuities ε_B, appear when (large-scale) dynamo action ceases; this behaviour is perhaps most noticeable for $E = 10^{-4}$ where the viscous dissipation shows a plateau in the vicinity of $\widetilde{Ra} \approx 25$, in which different values of $\widetilde{Ra}$ yield similar values of ε_u. This plateau is associated with a rapid increase in ε_B as the small-scale dynamo becomes activated. At a fixed value of $\widetilde{Ra}$ we observe scatter for different values of Pm which is

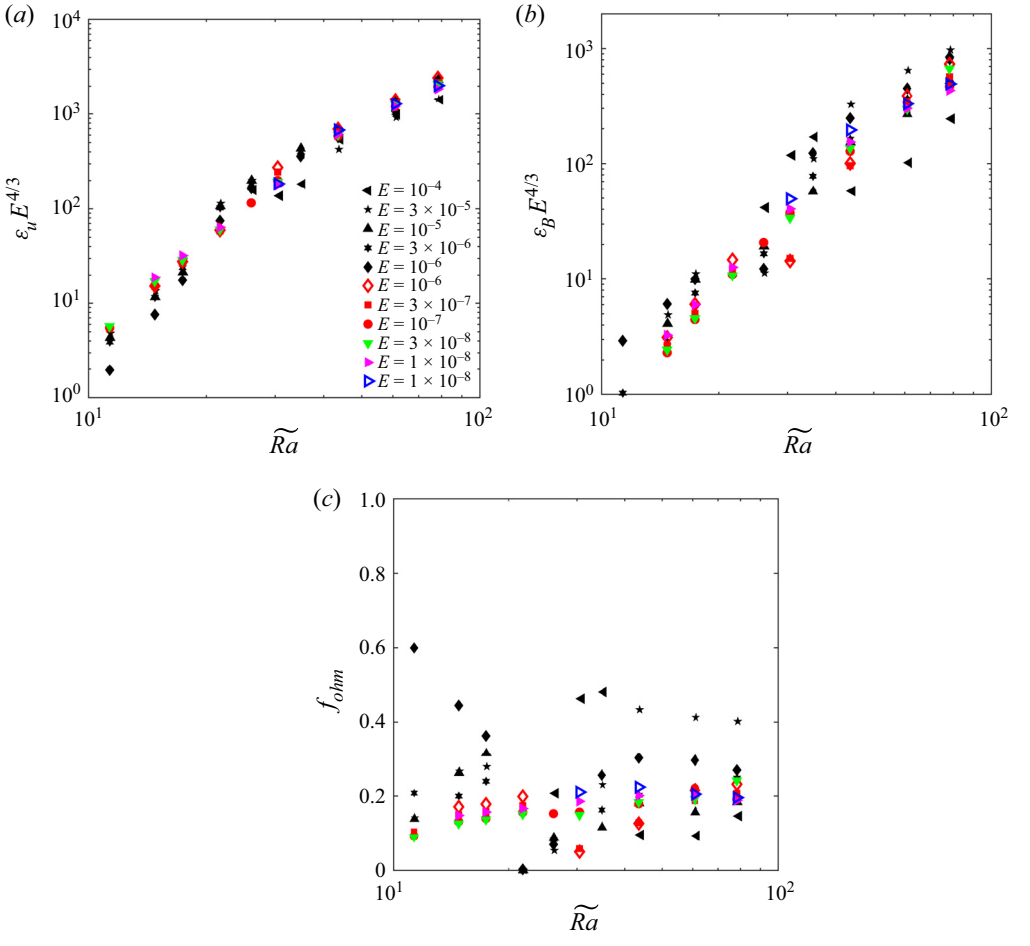

Figure 5. Dissipation as a function of reduced Rayleigh number $\widetilde{Ra}$ for all simulations: (*a*) rescaled viscous dissipation, $\varepsilon_u E^{4/3}$; (*b*) rescaled ohmic dissipation, $\varepsilon_B E^{4/3}$; (*c*) fraction of ohmic dissipation, $f_{ohm} = \varepsilon_B/(\varepsilon_B + \varepsilon_u)$. Symbol shape represents different values of the Ekman number (E) and colour represents different values of the magnetic (Pm): black indicates $Pm = 1$; red indicates $Pm = 0.3$; green indicates $Pm = 0.2$; magenta indicates $Pm = 0.1$; blue indicates $Pm = 0.05$.

related to the magnetic Reynolds number and the corresponding magnetic field behaviour (i.e. see figures 5 and 7).

We compute the relative size of the ohmic dissipation to the total dissipation using the fraction of ohmic dissipation, f_{ohm}, defined as

$$f_{ohm} = \frac{\varepsilon_B}{\varepsilon_B + \varepsilon_u}. \tag{4.1}$$

Figure 5(*c*) shows f_{ohm} vs $\widetilde{Ra}$. For the majority of our cases the flow is dominated by viscous dissipation ($\varepsilon_u > \varepsilon_B$), which is consistent with previous plane layer dynamo studies (Tilgner 2014). In the small-scale dynamo regime, the majority of our cases have a fraction of ohmic dissipation $f_{ohm} \sim 0.2$. In comparison with previous studies of dynamos in spherical geometries, we find f_{ohm} values that are relatively small. For instance, Schaeffer *et al.* (2017) find $f_{ohm} = 0.86$ with $Pm = 0.1$ and $E = 5 \times 10^{-8}$. The differences

in these values may be due to the differences in both magnetic field structure and saturation mechanisms in the two geometries.

4.3. *Velocity and magnetic field scaling*

Figure 6(*a*) shows the scaling behaviour of the Reynolds number, Re. For a fixed value of $\widetilde{Ra}$, the flow speed shows a systematic increase with decreasing Ekman number. We note that, for the $E = 10^{-4}$ and 3×10^{-5} cases, we observe a regime near $Ra \sim 3Ra_c$ ($\widetilde{Ra} \approx 26$) where the Reynolds number increases slowly (or remains constant) as Ra increases, while the Nusselt number still increases with increasing the Ra. Over this same parameter range we also observe a relatively large increase in the ohmic dissipation (as shown in figure 5*b*) and the magnetic energy (discussed in the next subsection), suggesting that the energy from the thermal forcing is transformed into magnetic energy very efficiently for these cases. The reduced Reynolds number, $\widetilde{Re} = ReE^{1/3}$, is plotted in figure 6(*b*) where a collapse is observed. Moreover, that these dynamos are characterised by $\widetilde{Re} = O(1)$ for a wide range of Ekman numbers suggests that the $Re = O\left(E^{-1/3}\right)$ scaling is the appropriate asymptotic relationship for describing the characteristic flow speeds. A change in the scaling behaviour of $\widetilde{Re}$ is observed around $Ra \sim 3Ra_c$ ($\widetilde{Ra} \sim 30$). For cases just above the onset of convection ($Ra < 3Ra_c$), an approximate scaling relation of $\widetilde{Re} \sim \widetilde{Ra}^2$ is found; while for cases with relatively high supercriticality ($Ra > 3Ra_c$), the scaling becomes weaker and a trend of $\widetilde{Re} \sim \widetilde{Ra}$ is shown for reference.

The magnetic Reynolds number Rm and rescaled magnetic Reynolds number $\widetilde{Rm} = RmE^{1/3}$ are shown in figures 6(*c*) and 6(*d*). Values of the magnetic Reynolds number up to $Rm \approx 3000$ are reached for $E = 10^{-6}$ and $Pm = 1$. The use of $\widetilde{Rm}$ in figure 6(*d*) shows how different values of Pm collapse onto different curves, although we find similar scaling behaviour with $\widetilde{Ra}$. For $Pm < 1$, the $\widetilde{Rm} < 1$ regime that is relevant to planetary interiors is accessible provided that the Ekman number is also reduced. We find that the regime where large-scale dynamo action is no longer important occurs at $\widetilde{Rm} \approx 5$; a value of $\widetilde{Rm} \approx 13.5$ for the transition was identified by Tilgner (2012), although larger values of Pm were employed in that investigation.

The magnetic energy E_{mag} and the rescaled magnetic energy $\tilde{E}_{mag} = E_{mag}E^{2/3}$ are shown in figures 7(*a*) and 7(*b*), respectively. For the majority of our cases, a smaller value of the Ekman number tends to produce a stronger magnetic field (as measured by the magnetic energy) when $\widetilde{Ra}$ and Pm are fixed. For all cases with $Pm = 1$, and cases with $Pm = 0.3$ and $E \geqslant 3 \times 10^{-7}$, there is either a significant drop in magnetic energy or a lack of dynamo action in the approximate range $20 \lesssim \widetilde{Ra} \lesssim 30$. This behaviour was also observed in the investigations of Tilgner (2012) and Guervilly *et al.* (2017) for $E \geqslant 10^{-6}$. However, this drop in magnetic energy becomes less significant or is not observed at all for cases with $E \lesssim 1 \times 10^{-7}$. Although we have not investigated this effect in detail, it appears that, as the Ekman number is reduced, the small-scale dynamo has already been fully activated once large-scale dynamo action ceases. As suggested in figure 7(*b*), a factor of $E^{2/3}$ appears to collapse the majority of the data to order-unity values, although significant scatter in the data remains due to differences in Pm and the corresponding dynamo behaviour.

The mean magnetic energy is shown in figure 7(*c*); the corresponding asymptotically rescaled data are shown in panel (*d*). In the large-scale dynamo regime, the mean magnetic energy appears to saturate and then decreases slightly as $\widetilde{Ra}$ increases. This behaviour is similar to that observed in spherical dynamo simulations, which show a saturation of the

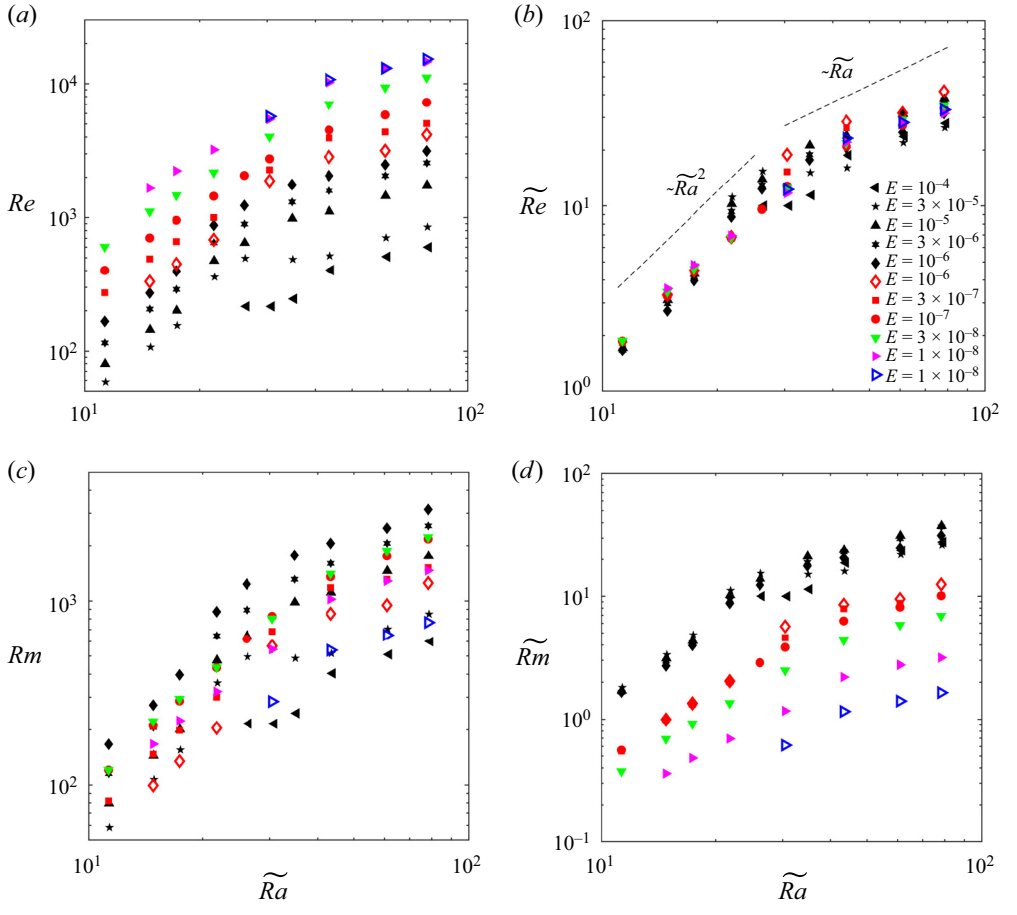

Figure 6. Reynolds number and magnetic Reynolds number vs reduced Rayleigh number $\widetilde{Ra}$: (*a*) large-scale Reynolds number, Re; (*b*) small-scale Reynolds number, $\widetilde{Re} = ReE^{1/3}$; (*c*) large-scale magnetic Reynolds number, Rm; (*d*) small-scale magnetic Reynolds number, $\widetilde{Rm} = RmE^{1/3}$. Symbol shape represents different values of the Ekman number (E) and colour represents different values of the magnetic (Pm): black indicates $Pm = 1$; red indicates $Pm = 0.3$; green indicates $Pm = 0.2$; magenta indicates $Pm = 0.1$; blue indicates $Pm = 0.05$.

axisymmetric component of the magnetic field (Calkins *et al.* 2021; Orvedahl *et al.* 2021). The exact cause of this effect is not currently known, but we speculate that it may be due to the breakdown of the α^2-dynamo that occurs at finite $\widetilde{Rm}$, perhaps related to so-called α-quenching (e.g. Vainshtein & Cattaneo 1992; Cattaneo & Hughes 1996). As shown in previous work (e.g. Steenbeck *et al.* 1966; Moffatt & Dormy 2019), dynamos can only be rigorously classified as α^2 if the small-scale magnetic Reynolds number is small. In the rapidly rotating limit in which significant separation exists between the small horizontal convective length scale and the layer depth, the requirement for an α^2-dynamo is that $\widetilde{Rm} \ll 1$ (Calkins *et al.* 2015). In contrast, for $\widetilde{Rm} = O(1)$ there is no rigorous closure relating the large- and small-scale magnetic field components.

We can further characterise the dynamos by plotting the ratio of the magnetic energy to the kinetic energy, as shown in figure 8. We find that the energy ratio is greater than unity only for relatively small Rayleigh numbers, $\widetilde{Ra} < 20$, indicating that kinetic energy dominates in the majority of our simulations. The decrease of this ratio with increasing

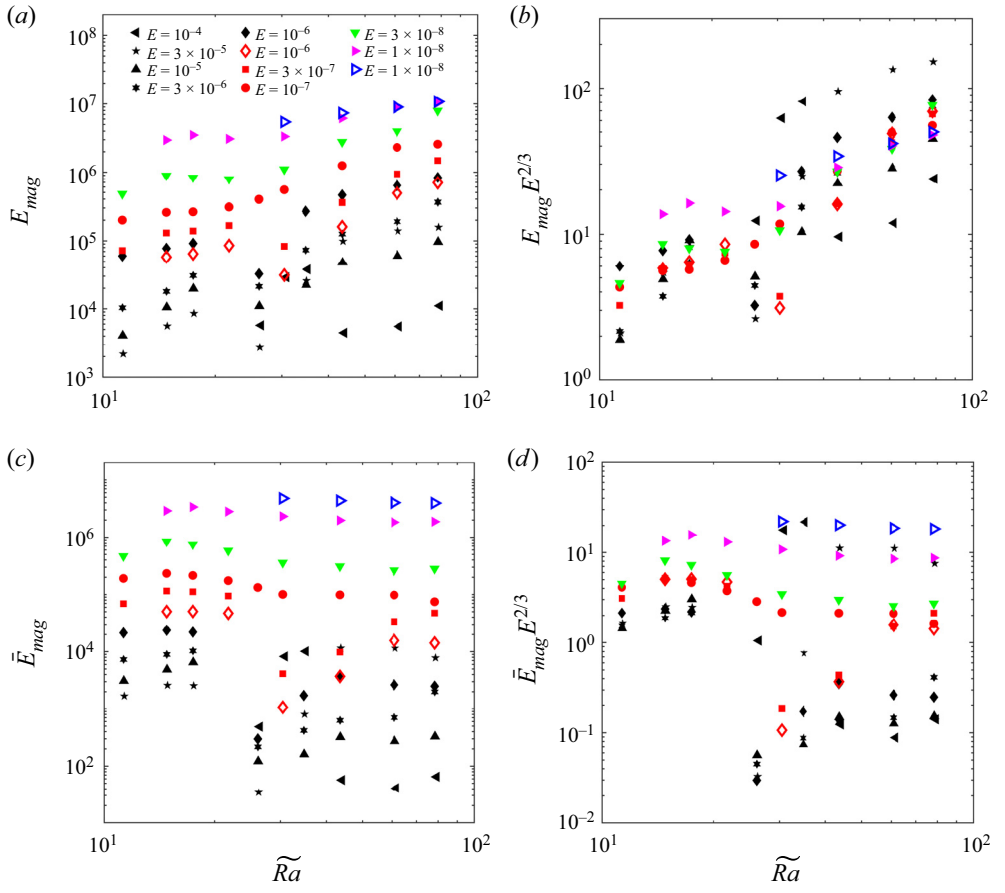

Figure 7. Magnetic energy for all simulations: (*a*) E_{mag} vs $\widetilde{Ra}$; (*b*) rescaled magnetic energy, $\tilde{E}_{mag} = E_{mag}E^{2/3}$, vs $\widetilde{Ra}$; (*c*) mean magnetic energy $\bar{E}_{mag}$ vs $\widetilde{Ra}$; (*d*) rescaled mean magnetic energy $\bar{E}_{mag}E^{2/3}$ vs $\widetilde{Ra}$. Symbol shape represents different values of the Ekman number (E) and colour represents different values of the magnetic (Pm): black indicates $Pm = 1$; red indicates $Pm = 0.3$; green indicates $Pm = 0.2$; magenta indicates $Pm = 0.1$; blue indicates $Pm = 0.05$.

$\widetilde{Ra}$ suggests that small-scale dynamos are more likely to yield smaller magnetic energy relative to kinetic energy. Within this small-scale dynamo regime we find many of the simulations have an energy ratio of $O(10^{-1})$.

The asymptotic theory predicts that the energy ratio becomes large in the limit $\widetilde{Rm} \to 0$. While we do find energy ratios that exceed unity, for computational reasons the majority of our simulations are within the regime $\widetilde{Rm} = O(1)$, so it might be expected that we do not observe large values of the energy ratio. In the Earth's outer core, $\widetilde{Rm} = O(10^{-2})$, and the energy ratio is thought to be as large as $\approx 10^4$. Spherical dynamo investigations find energy ratios that exceed those observed here, although these values rarely exceed 10. The reader is referred to Schaeffer *et al.* (2017) where a comparison of these values is made for several spherical dynamo investigations. A possible reason for the difference in values of this energy ratio for the two geometries may simply be related to the magnetic field morphology. Whereas spherical dynamos can generate large-scale fields in both the horizontal and vertical directions, the plane layer is only capable of generating a large-scale field in the horizontal direction.

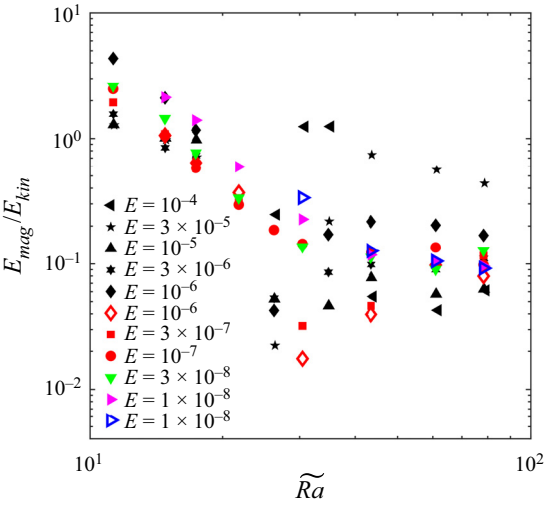

Figure 8. Ratio of magnetic energy to kinetic energy for all simulations. Symbol shape represents different values of the Ekman number (E) and colour represents different values of the magnetic (Pm): black indicates $Pm = 1$; red indicates $Pm = 0.3$; green indicates $Pm = 0.2$; magenta indicates $Pm = 0.1$; blue indicates $Pm = 0.05$.

4.4. *Length scales and energy spectra*

In this subsection we quantify the length scales present in both the velocity field and the magnetic field using a combination of energy spectra and Taylor microscales. This procedure is important for understanding how the length scales depend on the non-dimensional parameters. Both the kinetic and magnetic energy spectra are separated into horizontal and vertical components denoted by superscripts H and V, respectively. The spectra are averaged in time and depth. For example, the (time-averaged) kinetic energy spectra at depth z are defined as

$$\hat{E}^H_{kin}(k, z) = \frac{1}{2E^2} \sum_k (\hat{u}^* \hat{u} + \hat{v}^* \hat{v}), \tag{4.2}$$

and

$$\hat{E}^V_{kin}(k, z) = \frac{1}{2E^2} \sum_k (\hat{w}^* \hat{w}), \tag{4.3}$$

where $\hat{u}$, $\hat{v}$ and $\hat{w}$ are the Fourier coefficients of the three velocity field components, and the superscript $(*)$ denotes a complex conjugate. The horizontal wavenumber is $\boldsymbol{k} = (k_x, k_y)$, where the modulus is denoted by $k = \sqrt{k_x^2 + k_y^2}$. The corresponding depth-averaged spectra are then computed via

$$\hat{E}^H_{kin}(k) = \int_0^1 \hat{E}^H_{kin}(k, z)\, \mathrm{d}z, \tag{4.4}$$

and

$$\hat{E}^V_{kin}(k) = \int_0^1 \hat{E}^V_{kin}(k, z)\, \mathrm{d}z. \tag{4.5}$$

Asymptotically rescaled kinetic energy spectra are shown in figure 9 for two representative Rayleigh numbers: a relatively low value of $Ra = 1.7Ra_c$ ($\widetilde{Ra} \approx 15$) is

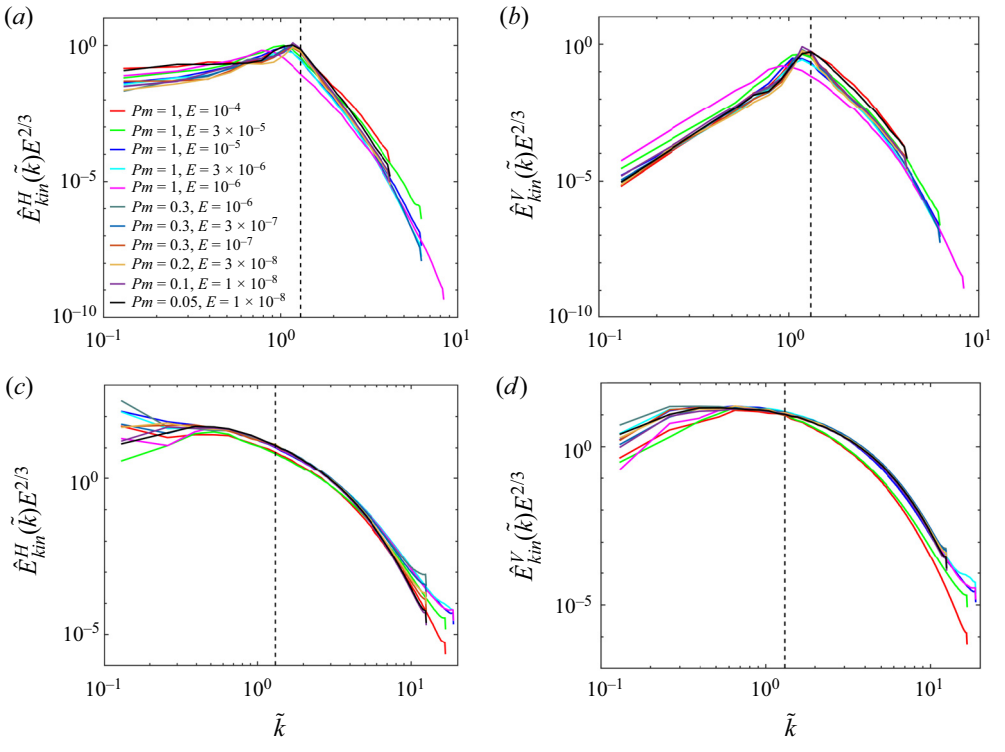

Figure 9. Asymptotically rescaled horizontal (*a*,*c*) and vertical (*b*,*d*) kinetic energy spectra for (*a*,*b*) $Ra = 1.7Ra_c$ ($\widetilde{Ra} \approx 15$) and (*c*,*d*) $Ra = 9Ra_c$ ($\widetilde{Ra} \approx 78$). The asymptotically rescaled horizontal wavenumber is defined by $\tilde{k} = kE^{1/3}$. The vertical dashed line denotes the asymptotically rescaled critical horizontal wavenumber, $\tilde{k}_c \approx 1.3048$.

shown in panels (*a*,*b*) and the highest Rayleigh number of $Ra = 9Ra_c$ ($\widetilde{Ra} \approx 78$) in shown in panels (*c*,*d*). As illustrated in figure 2, cases with $\widetilde{Ra} \approx 15$ can be considered quasi-laminar, whereas cases with $\widetilde{Ra} \approx 78$ are turbulent. The spectra are plotted in terms of the rescaled horizontal wavenumber, $\tilde{k} = kE^{1/3}$; the critical value of $\tilde{k}_c \approx 1.3048$ is shown by the dashed vertical line. The kinetic energy scaling of $\hat{E}^H_{kin}(k) \sim E^{-2/3}$ (or $\hat{E}^V_{kin}(k) \sim E^{-2/3}$) was given in (3.14). We note that all of the cases shown have qualitatively, and to some degree, quantitatively, similar behaviour across varying Ekman and magnetic Prandtl numbers. The collapse of the spectra in wavenumber space indicates that all length scales in the flow scale as $E^{1/3}$, even for turbulent flows. These similarities in the spectra are expected given the asymptotic state of the system (i.e. small Ekman and Rossby numbers). As expected, a peak in the spectra is observed near $\tilde{k}_c \approx 1.3048$ for cases near convection onset (i.e. $\widetilde{Ra} \approx 15$); by comparison the spectra for $\widetilde{Ra} \approx 78$ are flatter in the vicinity of $\tilde{k}_c$. Figure 9(*a*) shows that no dominant large-scale horizontal motion, as characterised by significant energy in the smallest wavenumbers, is observed near convection onset. On the other hand, figure 9(*b*) suggests that strong large-scale horizontal flows develop for sufficiently large $\widetilde{Ra}$, as indicated by the peak at the lowest rescaled wavenumber. We do not observe an obvious systematic influence of Pm on the kinetic energy spectra. For instance, whereas some cases with $Pm < 1$ show a tendency for LSV formation with a peak in the horizontal kinetic energy spectra at the smallest rescaled wavenumber, other cases with different Ekman numbers do not exhibit an obvious

signature of LSV formation. We note that when Pm and $\widetilde{Ra}$ are fixed, the large-scale horizontal motion appears to be suppressed as E decreases. Although we do not investigate this observation in detail, it is likely due the effect of magnetic damping on these flows (e.g. Guervilly *et al.* 2017; Maffei *et al.* 2019).

The magnetic energy equivalents of (4.4) and (4.5) are also computed and shown in figure 10. As for the kinetic energy spectra, we observe a collapse of the spectra with respect to the wavenumber scaling. In contrast to the kinetic energy spectra, there is considerably more spread in the rescaled magnitudes of the spectra, although the most energetic modes rescale approximately to $O(1)$ values. This spread is consistent with data reported in previous subsections. For instance, the relative size of the mean field varies considerably for a given value of $\widetilde{Ra}$ (and Pm). We notice that, for $\widetilde{Ra} \approx 15$, all of the dynamos show a peak in the horizontal spectra at the smallest value of $\widetilde{k}$, indicating the presence of a mean magnetic field. We observe two classes of dynamo spectra: cases with $Pm < 1$ show a steep drop in magnitude for $\widetilde{k} \gtrsim \widetilde{k}_c$, whereas cases with $Pm = 1$ show a much weaker drop in magnitude. At this same value of $\widetilde{Ra} \approx 15$, the corresponding vertical spectra show a nearly flat spectra for $\widetilde{k} \lesssim \widetilde{k}_c$, and a rapid drop in magnitude for $\widetilde{k} \gtrsim \widetilde{k}_c$. This distinction between spectra with $Pm < 1$ and those with $Pm = 1$ persists at $\widetilde{Ra} \approx 78$ shown in figures 10(*b*) and 10(*d*), although these higher Rayleigh number spectra are understandably more broadband in structure. The rapid drop in the spectra with increasing $\tilde{k}$ for $Pm < 1$ is expected when magnetic diffusion and mean field stretching balance in the fluctuating induction equation (Golitsyn 1960; Schekochihin *et al.* 2007).

The Taylor microscale for both the velocity field and the magnetic field are defined by, respectively,

$$\lambda_u = \sqrt{\frac{\langle \boldsymbol{u}^2 \rangle}{\langle (\boldsymbol{\nabla} \times \boldsymbol{u})^2 \rangle}}, \tag{4.6}$$

and

$$\lambda_B = \sqrt{\frac{\langle \boldsymbol{B'}^2 \rangle}{\langle (\boldsymbol{\nabla} \times \boldsymbol{B})^2 \rangle}}. \tag{4.7}$$

The corresponding asymptotically rescaled Taylor microscales are defined by

$$\tilde{\lambda}_u = \lambda_u E^{-1/3}, \quad \tilde{\lambda}_B = \lambda_B E^{-1/3}. \tag{4.8a,b}$$

The above definitions follow from assuming that the derivatives appearing in the definition of the Taylor microscales are dominated by the horizontal, $E^{-1/3}$ factor. Note that we use the fluctuating magnetic energy to calculate the magnetic Taylor microscale because we are interested in the length scale of the fluctuating magnetic field. On the other hand, we find that the dissipation contribution from the mean magnetic field is negligible compared with that from the fluctuating magnetic field. For simplicity, we therefore use the total dissipation in the calculations shown here.

Figures 11(*a*) and 11(*c*) show the velocity and magnetic Taylor microscales as a function of $\widetilde{Ra}$, respectively; the corresponding rescaled microscales are shown in panels (*b*,*d*). Good collapse is observed for both microscales when the $E^{-1/3}$ rescaling is applied, although this is to be expected in light of the collapse of the full spectra shown in figures 9 and 10. The rescaled velocity microscale is nearly constant over the range of investigated Rayleigh numbers; similar behaviour was found for a fixed value of E in a recent experimental study of rotating convection (Madonia *et al.* 2021). In contrast, we find two different regimes for λ_B, depending on the particular combination of Pm and $\widetilde{Ra}$,

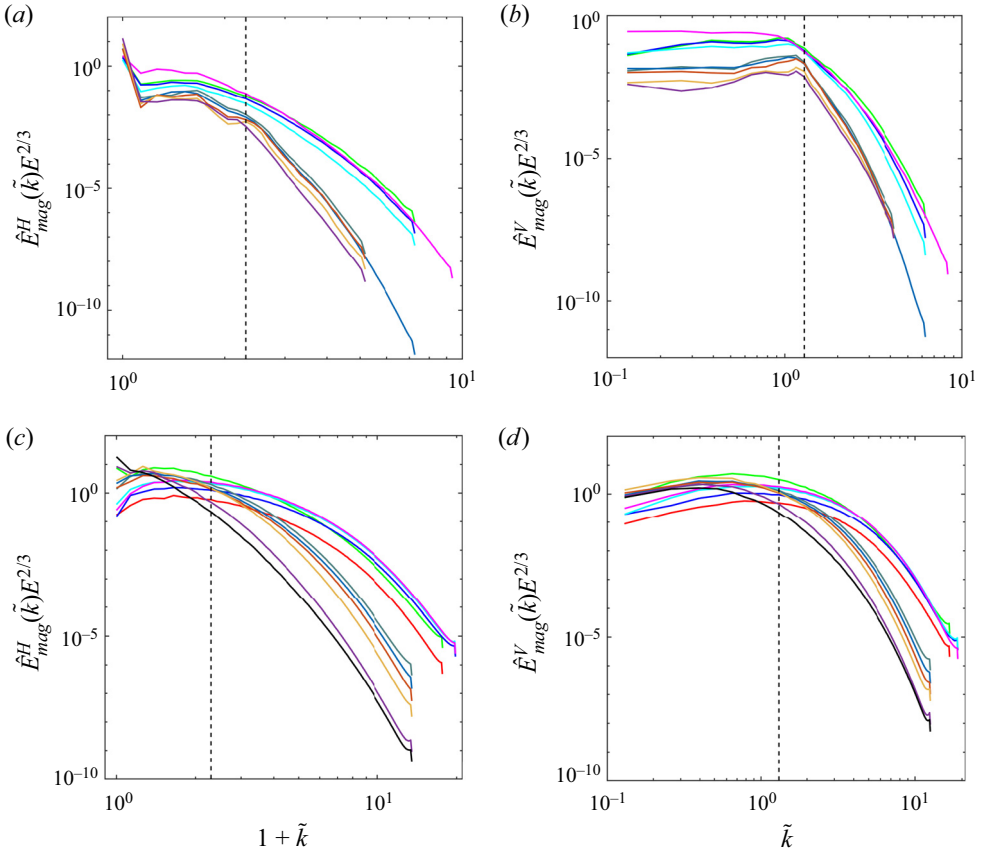

Figure 10. Asymptotically rescaled horizontal (*a*,*c*) and vertical (*b*,*d*) magnetic energy spectra for (*a*,*b*) $Ra = 1.7Ra_c$ ($\widetilde{Ra} \approx 15$) and (*b*,*d*) $Ra = 9Ra_c$ ($\widetilde{Ra} \approx 78$). The asymptotically rescaled horizontal wavenumber is defined by $\tilde{k} = kE^{1/3}$. The vertical dashed line denotes the asymptotically rescaled critical horizontal wavenumber, $\tilde{k}_c \approx 1.3048$. The colours have the same meaning as defined in figure 9.

as shown in figure 11(*d*). These regimes become more clear when plotted vs the reduced magnetic Reynolds number, $\widetilde{Rm}$, as shown in figure 11(*e*): when $\widetilde{Rm} \lesssim 3$ the magnetic microscale is nearly constant and we find $\lambda_B \sim \lambda_u$ (or equivalently $\tilde{\lambda}_B \sim \tilde{\lambda}_u$); for $\widetilde{Rm} \gtrsim 3$ we find $\lambda_B < \lambda_u$. This change in scaling behaviour can be attributed to the transition from large-scale dynamo action to small-scale dynamo action. As previously shown for the mean magnetic energy fraction, and suggested by theory (Calkins *et al.* 2015), this transition is well characterised by the size of $\widetilde{Rm}$.

The scaling behaviour of λ_B can be understood by considering the fluctuating induction equation

$$\partial_t \boldsymbol{B}' + \boldsymbol{u} \cdot \nabla \boldsymbol{B}' = \bar{\boldsymbol{B}} \cdot \nabla \boldsymbol{u} + \boldsymbol{B}' \cdot \nabla \boldsymbol{u} + \frac{E}{Pm} \nabla^2 \boldsymbol{B}'. \tag{4.9}$$

We assume that, in the small-scale dynamo regime, the large-scale magnetic field is small relative to the fluctuating magnetic field, $|\bar{\boldsymbol{B}}| \ll |\boldsymbol{B}'|$. As the magnetic Reynolds number increases the two terms on the left-hand side of (4.9) will tend to dominate, but the

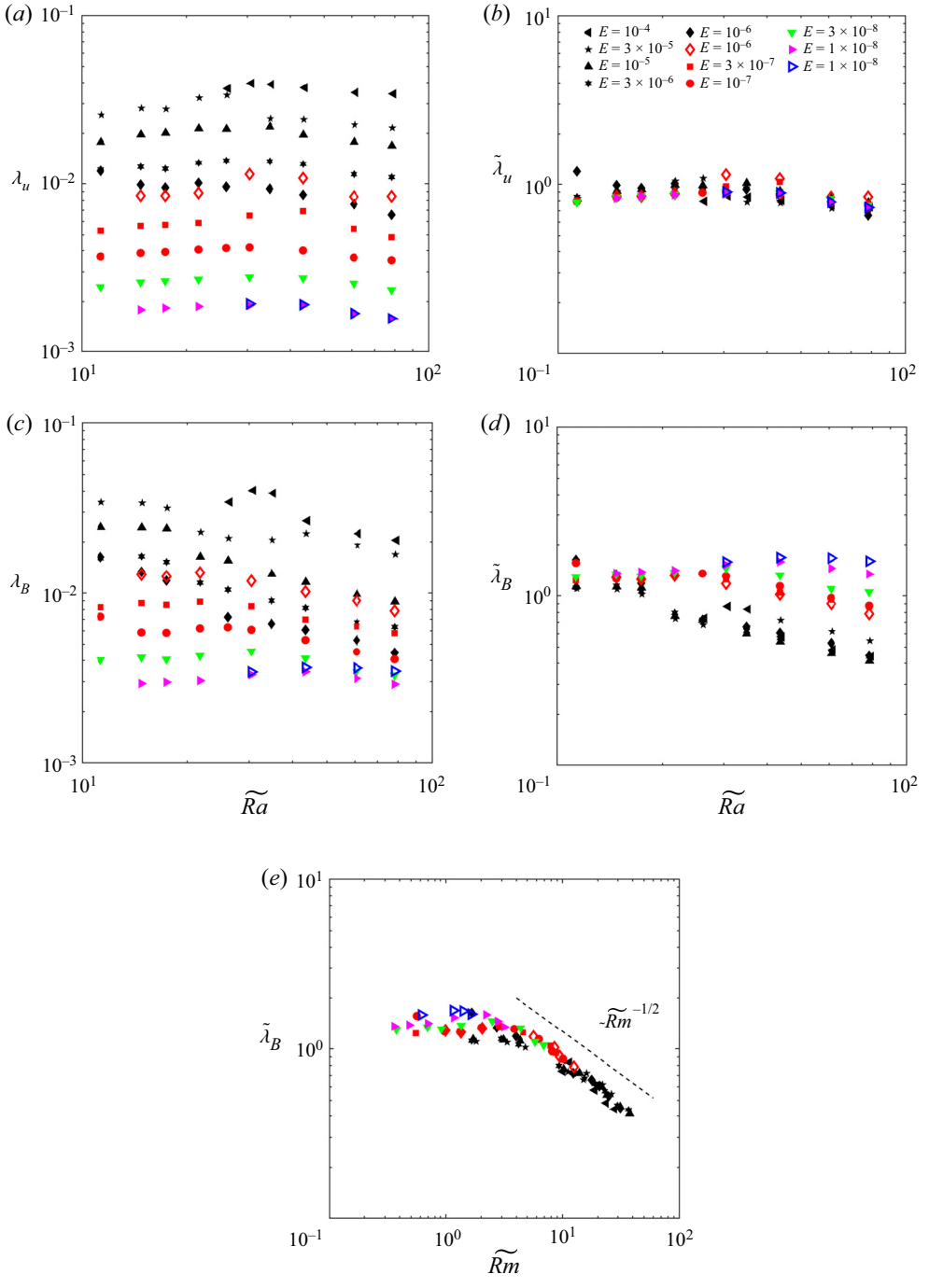

Figure 11. Taylor microscales for the velocity and magnetic fields: (*a*) velocity microscale vs $\widetilde{Ra}$; (*b*) rescaled velocity microscale ($\tilde{\lambda}_u = \lambda_u E^{-1/3}$) vs $\widetilde{Ra}$; (*c*) magnetic microscale vs $\widetilde{Ra}$; (*d*) rescaled magnetic microscale ($\tilde{\lambda}_B = \lambda_B E^{-1/3}$) vs $\widetilde{Ra}$; (*e*) rescaled magnetic microscale vs $\widetilde{Rm}$. Symbol shape represents different values of the Ekman number (E) and colour represents different values of the magnetic (Pm): black indicates $Pm = 1$; red indicates $Pm = 0.3$; green indicates $Pm = 0.2$; magenta indicates $Pm = 0.1$; blue indicates $Pm = 0.05$.

stretching and diffusion terms will reach a subdominant balance such that

$$\boldsymbol{B}' \cdot \boldsymbol{\nabla u} \sim \frac{E}{Pm}\nabla^2 \boldsymbol{B}' \quad \Rightarrow \quad \frac{U}{\lambda_u} \sim \frac{E}{Pm}\frac{1}{\lambda_B^2}. \tag{4.10}$$

Noting that U has units of the large-scale Rossby number we can use $U = ReE \sim \widetilde{Re}E^{2/3}$ such that

$$\lambda_B \sim E^{1/3}\widetilde{Rm}^{-1/2}, \tag{4.11}$$

which agrees with the observed scaling. These results suggest that the length scale of the magnetic field is controlled by both E and $\widetilde{Rm}$, depending on the particular regime. In terms of large-scale quantities, this suggests that the scaling behaviour of the ohmic dissipation scale in both the large-scale dynamo regime and the small-scale dynamo regime becomes

$$\text{Large-scale dynamo regime}: \quad \lambda_B \sim E^{1/3}, \tag{4.12}$$

$$\text{Small-scale dynamo regime}: \quad \lambda_B \sim Rm^{-1/2}E^{1/6}. \tag{4.13}$$

4.5. *Force balances*

In this subsection we numerically analyse the forces in the simulations. A similar analysis has been completed by Guzmán *et al.* (2021) for the hydrodynamic convection problem, although they did not consider the asymptotic scaling behaviour of the system. In comparison with Guzmán *et al.* (2021), our parameter space is restricted to the rapidly rotating regime. Here, we extend the force balance analysis to the dynamo problem and show that the asymptotic predictions of § 3 are consistent with the numerical data, confirming that dynamos in the plane layer geometry are QG in the limit of rapid rotation. Each force is denoted according to

$$\underbrace{\partial_t \boldsymbol{u}}_{F_t} = \underbrace{E\nabla^2\boldsymbol{u}}_{F_v} + \underbrace{(-\boldsymbol{u}\cdot\boldsymbol{\nabla u})}_{F_a} + \underbrace{(\boldsymbol{B}\cdot\boldsymbol{\nabla B})}_{F_l} + \underbrace{\frac{RaE^2}{Pr}\theta'\hat{\boldsymbol{z}}}_{F_b} + \underbrace{(-\hat{\boldsymbol{z}}\times\boldsymbol{u})}_{F_c} + \underbrace{(-\boldsymbol{\nabla}_\perp p' - \partial_z p'\hat{\boldsymbol{z}})}_{F_p}. \tag{4.14}$$

The hydrostatic balance in the vertical component of the momentum equation has been removed by defining the fluctuating pressure according to $p'(x, y, z, t) = p(x, y, z, t) - \bar{p}(z, t)$. In what follows we report time-averaged global root-mean-square (r.m.s.) values of the above forces.

Figure 12 shows r.m.s. values of the forces as a function of $\widetilde{Ra}$ for the specific case of $E = 1 \times 10^{-8}$ and $Pm = 0.1$. The horizontal components of the forces are shown in panel (*a*) and the vertical components are shown in panel (*b*). Other combinations of non-dimensional parameters were computed and show similar trends to the particular cases shown. For all cases, we find a dominant balance between the Coriolis force and the pressure gradient force in the horizontal dimensions, which suggests that all cases are in the QG dynamo regime. The global r.m.s. of the sum of the Coriolis and pressure gradient forces, defined by

$$F_c' = F_c + F_p, \tag{4.15}$$

is also shown and can be considered the ageostrophic component of the Coriolis force. As expected from QG theory this ageostrophic component is comparable in magnitude to all other terms in the (horizontal) momentum equation. Near the onset of convection we find that all of the subdominant terms are of the same order of magnitude; as $\widetilde{Ra}$

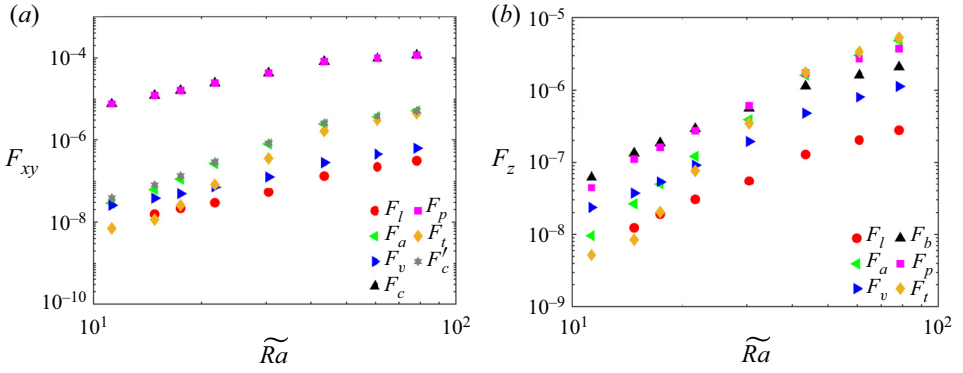

Figure 12. Global r.m.s. values of all forces for cases with $E = 1 \times 10^{-8}$ and $Pm = 0.1$. (*a*) The r.m.s. forces in the horizontal direction vs $\widetilde{Ra}$; (*b*) r.m.s. forces in the vertical direction vs $\widetilde{Ra}$. Note that the data points for the Coriolis and pressure gradient forces are directly on top of one another in panel (*a*).

is increased we find that advection, inertia and F_c' become larger in magnitude than the viscous force and the Lorentz force. In particular, we find that inertia becomes one of the largest subdominant terms for $\widetilde{Ra} \gtrsim 40$, suggesting that these flows become fully turbulent for Rayleigh numbers larger than this value. These observations suggest that the system enters a state that is well described by the so-called Coriolis–inertia–Archimedean balance (e.g. Jones 2015), although further investigation is necessary to confirm if the dominant length scales that arise in the system are consistent with this balance. The Lorentz force and viscous force remain comparable in magnitude over the investigated range of $\widetilde{Ra}$, although we find the differences are larger in the vertical component of the momentum equation, as shown in panel (*b*). Non-rotating dynamos also exhibit an approximate balance between the Lorentz and viscous forces (Yan *et al.* 2021). The buoyancy force and the vertical pressure gradient force remain the largest terms in the vertical component of the momentum equation for $\widetilde{Ra} \lesssim 40$; for larger $\widetilde{Ra}$ we find that inertia, advection and the pressure gradient force dominate.

A comparison of forces for a selection of different Ekman numbers (and different Pm) is made in figure 13. Here, we plot (*a*,*b*) the viscous force; (*c*,*d*) the Lorentz force; and (*e*,*f*) the buoyancy force for Ekman numbers $E = 10^{-5}$ ($Pm = 1$), 10^{-6} ($Pm = 1$), 10^{-7} ($Pm = 0.3$) and 10^{-8} ($Pm = 0.1$). The left column of the figure shows the unscaled data and the right column shows the asymptotically rescaled data. The forces show a good collapse when rescaled via the asymptotic predictions of § 3. Of the three forces shown, the Lorentz force shows the most scatter, which can be attributed to different values of Pm (or, equivalently, $\widetilde{Rm}$). As shown in panel (*f*), varying Pm has no significant effect on the scaling behaviour of either the viscous force or the buoyancy force.

5. Discussion

A systematic numerical investigation of convection-driven dynamos in the rotating plane layer geometry has been carried out for varying Ekman number, Rayleigh number and magnetic Prandtl number. The observed flow regimes ranged from quasi-laminar convection cells to geostrophic turbulence, similar to the regimes found in hydrodynamic rotating convection (e.g. Julien *et al.* 2012). A primary purpose of this investigation was to test the asymptotic theory developed by Calkins *et al.* (2015). In this regard, a variety of physical quantities were computed across the entire range of input parameters

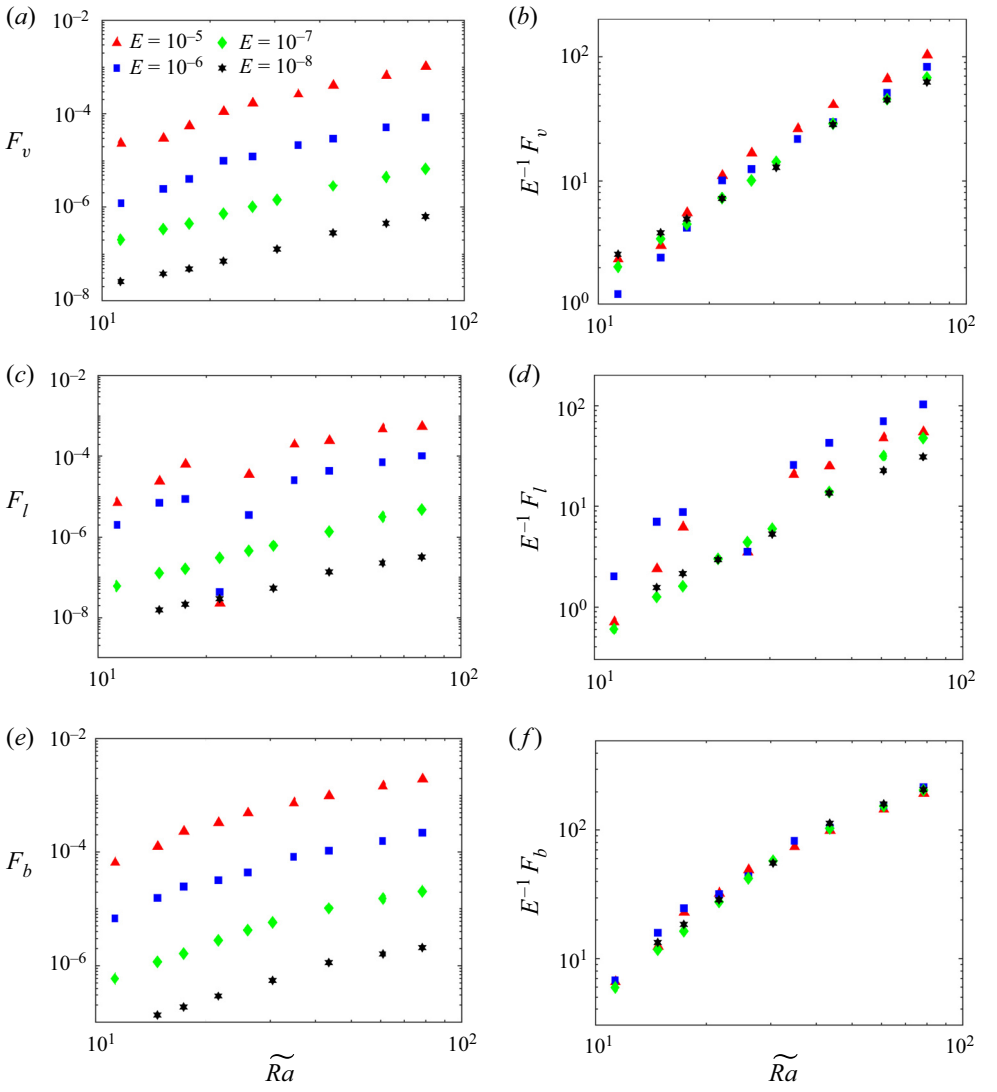

Figure 13. Scaling behaviour of (*a*,*b*) the viscous force; (*c*,*d*) the Lorentz force; and (*e*,*f*) the buoyancy force for different Ekman numbers. Panels (*a*,*c*,*e*) show the unscaled forces and (*b*,*d*,*f*) show the asymptotically rescaled forces. The markers have the same meaning in all figures.

to characterise the asymptotic scaling behaviour of the system. In general, excellent agreement between theory and simulation output was found.

The observed heat transport behaviour in the dynamo simulations is broadly similar to that observed in hydrodynamic rotating convection. More specifically, as a function of Rayleigh number, the Nusselt number initially grows quickly, then a more shallow slope is observed once the flow becomes turbulent. When plotted as a function of the reduced Rayleigh number $\widetilde{Ra} = RaE^{4/3}$, we find that the Nusselt number shows qualitatively, and even quantitatively, similar behaviour for all Ekman numbers and magnetic Prandtl numbers. As expected from the energy balance, the viscous and ohmic dissipation also show similar behaviour with increasing $\widetilde{Ra}$ and the dissipation data can be collapsed with a scaling of $E^{4/3}$. In the majority of the dynamos simulated, viscous dissipation

dominates over ohmic dissipation. In the turbulent regime, the ohmic dissipation fraction is $f_{ohm} \lesssim 0.5$ for the majority of the cases. This behaviour should be contrasted with spherical dynamo studies (Christensen & Aubert 2006), or magnetoconvection studies (Yan *et al.* 2019), where regimes can be found in which ohmic dissipation dominates over viscous dissipation.

Momentum transport, as characterised by the large-scale Reynolds number, scales with the Ekman number according to $E^{-1/3}$, consistent with asymptotic theory (Julien *et al.* 1998; Calkins *et al.* 2015). This scaling behaviour is a direct result of the geostrophic balance that occurs on the small, horizontal convective length scale. Although we do not attempt to provide detailed numerical fits to the data, the Reynolds number increases steeply for small $\widetilde{Ra}$, then transitions to a shallower scaling in the turbulent regime (beyond values of $\widetilde{Ra} \approx 40$), which is roughly consistent with asymptotic studies of non-magnetic rotating convection (e.g. Julien *et al.* 2012; Calkins *et al.* 2016; Maffei *et al.* 2021).

The magnetic energy of the simulated dynamos shows considerable scatter with the various input parameters, although a scaling of $E^{-2/3}$, as predicted by theory, provides some collapse to the data. We show that a near unity mean magnetic energy fraction, $\bar{E}_{mag}/E_{mag} \approx 1$, is obtainable so long as the Ekman number is small and $Pm < 1$. It is shown that the asymptotically scaled magnetic Reynolds number, $\widetilde{Rm} = RmE^{1/3}$, controls the value $\bar{E}_{mag}/E_{mag}$, and distinguishes dynamos dominated (energetically) by the large-scale magnetic field, from those dominated by the small-scale magnetic field. It is well known that large-scale magnetic fields can be generated when the magnetic Reynolds number is sufficiently small and the flow is coherent, i.e. laminar (e.g. Moffatt & Dormy 2019). Small values of $\widetilde{Rm}$ indicate that magnetic diffusion is important on the small convective length scales. Here, we find that robust large-scale magnetic field can readily be generated even in the presence of incoherent, turbulent flows (Yan & Calkins 2022), provided $\widetilde{Rm}$ remains small. In rough agreement with Tilgner (2012), small-scale dynamos are consistently achieved when $\widetilde{Rm} \gtrsim 1$.

The mean magnetic field shows a saturation with increasing Rayleigh number, despite the fact that the fluctuating magnetic field and associated electromotive force (e.m.f.) grow with increasing $\widetilde{Ra}$. Similar behaviour of the mean magnetic field is observed in spherical dynamos, where the azimuthally averaged component of the magnetic field shows a saturation with Rayleigh number (Calkins *et al.* 2021; Orvedahl *et al.* 2021). The exact cause of this saturation is not currently known, but it may be due to a breakdown of the α^2-dynamo mechanism that operates only when $\widetilde{Rm} \lesssim O(1)$ (Calkins *et al.* 2015). However, further investigation is necessary to confirm this hypothesis.

Linear theory predicts that the horizontal length scale at the onset of rotating convection scales with the Ekman number as $E^{1/3}$ in the limit $E \to 0$ (Chandrasekhar 1961). Whether these scales persist in the turbulent regime has remained an open question. Our analysis of both the kinetic and magnetic energy spectra suggests that all length scales in the velocity field and fluctuating magnetic field scale predominantly as $E^{1/3}$, even in the turbulent regime ($\widetilde{Ra} \gtrsim 40$). The viscous dissipation length scale (Taylor microscale) and the ohmic dissipation length scale are computed from these spectra and show good collapse when rescaled with $E^{1/3}$. The viscous dissipation length scale is approximately constant across a broad range of Rayleigh numbers – this behaviour has also been observed in hydrodynamic rotating convection experiments (Madonia *et al.* 2021). The ohmic dissipation length scale is approximately constant (and of the same order as the viscous dissipation length scale) within the large-scale dynamo regime, but transitions to a $\widetilde{Rm}^{-1/2}$ scaling in the small-scale dynamo regime.

All of the dynamos within our suite of simulations show a leading-order geostrophic force balance, with all other forces, including the Lorentz force, acting as perturbations. Thus, the simulated dynamos are within a QG dynamical state. Of course, the relative sizes of the various perturbing forces is fundamental to the resulting QG dynamics. We find that the Lorentz force tends to be approximately equal in magnitude to the viscous force across the entire range of investigated parameters; this behaviour is similar to that observed in non-rotating convection-driven dynamos (Yan *et al.* 2021).

It is often assumed that the amplitude of the magnetic field generated by a rapidly rotating dynamo will saturate once the Lorentz force becomes comparable in magnitude to the Coriolis force (e.g. Fautrelle & Childress 1982; Roberts 1988). For the QG dynamos studied here, such a balance does not occur at leading order, although a higher-order balance can take place in which the Lorentz force becomes comparable in magnitude to the ageostrophic component of the Coriolis force (e.g. Calkins 2018). However, since all forces in the momentum equation are of comparable magnitude at this perturbative order of the dynamics, it is less clear whether the comparison of the Lorentz force with only the Coriolis force is meaningful. In particular, for a fixed Ekman number, our simulations show that inertia becomes important in the turbulent regime. Further investigation, perhaps at a fixed small value of the Ekman number, and finer-scale variations of the Rayleigh number would help to isolate the effects of these perturbing forces.

Several previous studies have examined the relative sizes of the terms in the vorticity equation in both spherical (Dormy 2016) and plane layer dynamos (Hughes & Cattaneo 2016; Cattaneo & Hughes 2017; Hughes & Cattaneo 2019). These studies focused on so-called 'strong-field' dynamos in which the curl of the Lorentz force balances the vortex stretching term. In order to reach this balance it is typically necessary to use relatively large values of Pm (Dormy 2016) or to neglect inertia in the momentum equation (Hughes & Cattaneo 2016; Cattaneo & Hughes 2017; Hughes & Cattaneo 2019), since the relative size of inertia will grow with increasing Rayleigh number and eventually dominate the Lorentz force, as observed in the present study. Given the linearity of the momentum equation when inertia is absent, Hughes & Cattaneo (2019) decomposed the velocity field into 'thermal' and 'magnetic' components. Their analysis showed that whereas viscosity was small relative to buoyancy and the Coriolis terms in the thermal component of the vorticity equation, viscosity remained significant in the corresponding magnetic component. This observation is roughly consistent with our own results which show that the viscous force and the Lorentz force are comparable to one another.

It is well known that in homogenous, isotropic turbulence the largest eddies present in the flow tend to control the viscous dissipation rate such that the Taylor microscale is a strongly decreasing function of the Reynolds number (e.g. Pope 2000). Indeed, this behaviour is observed in non-rotating Rayleigh–Bénard convection and the corresponding dynamos (e.g. Yan *et al.* 2021). That the dissipation length scales in our simulations, and those in the hydrodynamic study of Madonia *et al.* (2021), do not change appreciably with the Rayleigh number indicates that rotationally constrained convective turbulence behaves very differently in comparison with non-rotating convection. This difference may simply be due to the fact that a small, viscous length scale is necessary in order to overcome the constraints imposed by rotation, as is known from linear theory. Provided that the Rossby and Ekman number are both small, the convection remains geostrophically balanced even in the turbulent regime. We stress that the predominance of the $E^{1/3}$ viscous length scale does not require that the viscous force is the largest perturbative force. Indeed, the simulations show that other perturbative forces such as inertia can

become larger than the viscous force as the Rayleigh number is increased. However, this perturbation of the geostrophic balance can still occur on the $E^{1/3}$ length scale. One might argue that the predominance of the $E^{1/3}$ length scale suggests that the Rayleigh numbers (or, equivalently, the Reynolds numbers) accessible in the present simulations are not sufficiently large to access the fully turbulent regime. However, there are two problems with this view. First, to our knowledge, the present set of simulations represent the most extreme DNS of either rotating convection or rotating convection-driven dynamos carried out to date, as based on the combination of Ekman numbers and Reynolds numbers. While the possibility remains that an additional transition in the dynamics might appear at larger Rayleigh numbers (and perhaps smaller Ekman numbers), simulations of the QG model for hydrodynamic rotating convection do not observe such a transition up to $\widetilde{Ra} = 200$ (Maffei *et al.* 2021).

The present investigation highlights significant differences between rotating dynamos in the plane geometry and those that occur in spherical geometries. Some of these differences include the observed sequence of force balances and the relative magnitude of the Lorentz force, and the number of asymptotically distinct convective length scales. It is typical to define the large-scale fields in a spherical domain as a zonal average, and small scales as fluctuations away from this average. On the small scales, the leading-order force balance is geostrophic in spherical geometries, with the Lorentz force and buoyancy force entering at the next (higher) order in the dynamics, and all other forces are smaller still (Yadav *et al.* 2016). In contrast, simulations show that the large-scale dynamics in spherical dynamos is semi-magnetostrophic with a thermal wind balance in the meridional plane and a Coriolis–Lorentz force balance in the zonal direction (Aubert 2005; Calkins *et al.* 2021). This latter balance allows for saturation of the large-scale magnetic field via the Malkus–Proctor mechanism (Malkus & Proctor 1975). However, no equivalent saturation mechanism for the large-scale magnetic field is present in the plane layer geometry. The linear theory of rotating convection in spherical shells shows the presence of two asymptotically distinct convective length scales – one is the familiar $E^{1/3}$ zonal length and the other is the $E^{2/9}$ radial length scale (Dormy *et al.* 2004). The influence of different length scales, and the associated anisotropy in the fluctuating velocity field, may play a role in the different sequence of force balances that are observed in the two geometries, although further investigation is necessary to test this hypothesis.

Funding. This paper benefited greatly from comments made by three anonymous referees. The authors gratefully acknowledge funding from the National Science Foundation (NSF) through grants EAR-1945270 and SPG-1743852. The computations were carried out on the Summit and Stampede2 supercomputers. Summit is supported by NSF awards ACI-1532235 and ACI-1532236, the University of Colorado Boulder and Colorado State University. Stampede2 is operated by the Texas Advanced Computing Center (TACC) and was made available through Extreme Science and Engineering Discovery Environment (XSEDE) allocation PHY180013. Flow visualisation was performed with VAPOR (Li *et al.* 2019).

Declaration of interests. The authors report no conflict of interest.

Author ORCIDs.
Michael A. Calkins https://orcid.org/0000-0002-6917-5365.

Appendix. Simulation data

https://doi.org/10.1017/jfm.2022.848 Published online by Cambridge University Press

E	$\widetilde{Ra}$	$N_x \times N_y \times N_z$	Δt	Nu	Re	Rm	E_{mag}	$\bar{E}_{mag}/E_{mag}$	λ_u	λ_B
1×10^{-4}	11.45	$96 \times 96 \times 48$	2	1.55	41.6	41.6	—	—	0.0358	—
1×10^{-4}	14.97	$96 \times 96 \times 48$	0.5	2.65	85.9	85.9	—	—	0.0373	—
1×10^{-4}	17.61	$96 \times 96 \times 48$	0.4	3.87	125.8	125.8	—	—	0.0381	—
1×10^{-4}	22.01	$144 \times 144 \times 72$	0.2	6.16	205.3	205.3	—	—	0.0416	—
1×10^{-4}	26.42	$144 \times 144 \times 72$	0.08	8.61	215.9	215.9	5.8×10^3	0.0846	0.0369	0.0343
1×10^{-4}	30.82	$192 \times 192 \times 108$	0.02	9.25	215.6	215.6	2.9×10^4	0.2859	0.0397	0.0403
1×10^{-4}	35.22	$192 \times 192 \times 108$	0.01	11.00	245.9	245.9	3.8×10^4	0.2691	0.0391	0.0388
1×10^{-4}	44.03	$192 \times 192 \times 144$	0.01	14.59	403.9	403.9	4.5×10^3	0.0128	0.0373	0.0267
1×10^{-4}	61.64	$288 \times 288 \times 288$	0.005	18.67	509.4	509.4	5.6×10^3	0.0074	0.0349	0.0224
1×10^{-4}	79.25	$384 \times 384 \times 288$	0.003	21.99	600.5	600.5	1.1×10^4	0.0059	0.0343	0.0205
3×10^{-5}	11.37	$96 \times 96 \times 48$	2	1.49	58.4	41.6	2.18×10^3	0.7712	0.0257	0.0343
3×10^{-5}	14.87	$144 \times 144 \times 72$	0.4	2.24	107.2	107.2	5.6×10^3	0.4621	0.0282	0.0339
3×10^{-5}	17.49	$144 \times 144 \times 72$	0.2	3.30	155.2	155.2	8.6×10^3	0.2984	0.0278	0.0317
3×10^{-5}	21.86	$144 \times 144 \times 72$	0.15	6.22	358.9	358.9	—	0.0110	0.0325	—
3×10^{-5}	26.23	$192 \times 192 \times 108$	0.08	9.08	495.2	495.2	2.7×10^3	0.0125	0.0337	0.210
3×10^{-5}	34.98	$192 \times 192 \times 144$	0.015	14.65	485.8	485.8	2.6×10^4	0.0312	0.0244	0.0205
3×10^{-5}	43.72	$216 \times 216 \times 216$	0.005	17.94	515.8	515.8	9.9×10^4	0.1170	0.0242	0.0224
3×10^{-5}	61.21	$288 \times 288 \times 288$	0.002	25.27	705.0	705.0	1.3×10^5	0.0825	0.0225	0.0192
3×10^{-5}	78.70	$384 \times 384 \times 324$	0.001	31.56	849.1	849.1	1.58×10^5	0.0496	0.0215	0.0169

Table 1. Details of the numerical simulations for $Pm = 1$, $E = (1 \times 10^{-4}, 3 \times 10^{-5})$ cases. The non-dimensional parameters are the reduced Rayleigh number $\widetilde{Ra}$, the Nusselt number Nu, the Reynolds number Re and the magnetic Reynolds number Rm. The spatial resolution is quoted in terms of the de-aliased physical space grid points $N_x \times N_y \times N_z$, where (N_x, N_y) is the horizontal resolution and N_z is the vertical resolution. The numerical timestep size is denoted by Δt. The magnetic energy is denoted by E_{mag}, and the velocity Taylor microscale and magnetic Taylor microscale are denoted by λ_u and λ_B, respectively.

https://doi.org/10.1017/jfm.2022.848 Published online by Cambridge University Press

E	$\widetilde{Ra}$	$N_x \times N_y \times N_z$	Δt	Nu	Re	Rm	E_{mag}	$\bar{E}_{mag}/E_{mag}$	λ_u	λ_B
1×10^{-5}	11.33	$96 \times 96 \times 72$	1	1.45	79.5	79.5	4.1×10^3	0.7616	0.0177	0.0245
1×10^{-5}	14.82	$144 \times 144 \times 72$	0.4	2.07	144.3	144.3	1.1×10^4	0.4637	0.0197	0.0243
1×10^{-5}	17.44	$144 \times 144 \times 72$	0.2	2.80	200.7	200.7	2.0×10^4	0.3320	0.0201	0.0240
1×10^{-5}	21.80	$144 \times 144 \times 96$	0.2	5.86	474.8	474.8	—	—	0.0213	—
1×10^{-5}	26.16	$192 \times 192 \times 108$	0.1	9.41	646.8	646.8	1.1×10^4	0.0111	0.0212	0.156
1×10^{-5}	34.88	$192 \times 192 \times 144$	0.015	15.09	982.9	982.9	2.2×10^4	0.0072	0.0219	0.0129
1×10^{-5}	43.60	$216 \times 216 \times 216$	0.006	20.19	1.11×10^3	1.11×10^3	4.8×10^4	0.0067	0.0196	0.0116
1×10^{-5}	61.03	$432 \times 432 \times 384$	0.002	28.34	1.45×10^3	1.45×10^3	6.1×10^4	0.0045	0.0178	0.0099
1×10^{-5}	78.47	$432 \times 432 \times 480$	0.0008	34.89	1.75×10^3	1.75×10^3	9.7×10^4	0.0034	0.0168	0.0089
3×10^{-6}	11.32	$96 \times 96 \times 96$	0.5	1.43	115.3	115.3	1.0×10^4	0.7055	0.0121	0.0161
3×10^{-6}	14.80	$144 \times 144 \times 96$	0.4	1.97	206.0	206.0	1.8×10^4	0.4986	0.0126	0.0165
3×10^{-6}	17.41	$240 \times 240 \times 96$	0.2	2.67	289.4	289.4	3.1×10^4	0.3363	0.0123	0.0153
3×10^{-6}	21.77	$144 \times 144 \times 108$	0.1	5.38	647.5	647.5	—	0.0133	0.0133	—
3×10^{-6}	26.12	$192 \times 192 \times 144$	0.1	8.71	893.5	893.5	2.1×10^4	0.0102	0.0137	0.0105
3×10^{-6}	34.83	$288 \times 288 \times 288$	0.01	15.63	1.31×10^3	1.31×10^3	7.4×10^4	0.0057	0.0136	0.0090
3×10^{-6}	43.53	$288 \times 288 \times 384$	0.006	20.25	1.60×10^3	1.60×10^3	1.3×10^5	0.0050	0.0131	0.0082
3×10^{-6}	60.94	$432 \times 432 \times 576$	0.002	31.19	2.06×10^3	2.06×10^3	1.9×10^5	0.0037	0.0114	0.0067
3×10^{-6}	78.36	$432 \times 432 \times 648$	0.0006	41.06	2.56×10^3	1.75×10^3	3.6×10^5	0.0055	0.0109	0.0063
1×10^{-6}	11.31	$96 \times 96 \times 96$	0.5	1.46	166.6	166.6	6.0×10^4	0.3538	0.0119	0.0163
1×10^{-6}	14.79	$192 \times 192 \times 192$	0.4	1.93	271.9	271.9	7.8×10^4	0.3047	0.0099	0.0133
1×10^{-6}	17.40	$288 \times 288 \times 192$	0.1	2.59	396.8	396.8	9.2×10^4	0.2393	0.0095	0.0118
1×10^{-6}	21.75	$144 \times 144 \times 192$	0.05	5.05	874.4	874.4	—	0.0163	0.0101	—
1×10^{-6}	26.10	$192 \times 192 \times 144$	0.1	7.77	1.23×10^3	1.23×10^3	3.2×10^4	0.0092	0.0096	0.0072
1×10^{-6}	34.80	$324 \times 324 \times 384$	0.01	14.80	1.77×10^3	1.77×10^3	2.7×10^5	0.0064	0.0093	0.0066
1×10^{-6}	43.50	$432 \times 432 \times 432$	0.006	20.58	2.06×10^3	2.06×10^3	4.6×10^5	0.0077	0.0086	0.0061
1×10^{-6}	60.90	$432 \times 432 \times 576$	0.0005	29.97	2.49×10^3	2.49×10^3	6.3×10^5	0.0042	0.0076	0.0053
1×10^{-6}	78.31	$432 \times 432 \times 768$	0.0005	47.10	3.15×10^3	1.75×10^3	8.3×10^5	0.0030	0.0066	0.0044

Table 2. Details of the numerical simulations for $Pm = 1$, $E = (1 \times 10^{-5}, 3 \times 10^{-6}, 1 \times 10^{-6})$ cases.

https://doi.org/10.1017/jfm.2022.848 Published online by Cambridge University Press

E	$\widetilde{Ra}$	$N_x \times N_y \times N_z$	Δt	Nu	Re	Rm	E_{mag}	$\bar{E}_{mag}/E_{mag}$	λ_u	λ_B
1×10^{-6}	11.31	$96 \times 96 \times 96$	8	1.57	194.7	58.4	—	—	0.0077	—
1×10^{-6}	14.79	$96 \times 96 \times 96$	2	2.24	331.5	99.5	5.8×10^4	0.8667	0.0085	0.0129
1×10^{-6}	17.40	$96 \times 96 \times 96$	1	2.88	449.0	134.7	6.5×10^4	0.7808	0.0085	0.0125
1×10^{-6}	21.75	$96 \times 96 \times 96$	0.5	4.41	681.6	204.5	8.5×10^4	0.5493	0.0088	0.0132
1×10^{-6}	30.45	$96 \times 96 \times 162$	0.1	10.52	1.89×10^3	566.2	3.1×10^4	0.0343	0.0114	0.0118
1×10^{-6}	43.50	$192 \times 192 \times 240$	0.01	18.62	2.84×10^3	852.9	1.6×10^5	0.0232	0.0108	0.0102
1×10^{-6}	60.90	$216 \times 216 \times 432$	0.005	30.64	3.16×10^3	948.9	4.9×10^5	0.0320	0.0084	0.0090
1×10^{-6}	78.31	$288 \times 288 \times 576$	0.003	40.39	4.17×10^3	1.25×10^3	6.9×10^5	0.0205	0.0084	0.0079
3×10^{-7}	11.31	$96 \times 96 \times 96$	8	1.53	273.5	82.0	7.2×10^4	0.9563	0.0053	0.0083
3×10^{-7}	14.79	$144 \times 144 \times 144$	2	2.20	490.0	147.0	1.30×10^5	0.8837	0.0056	0.0087
3×10^{-7}	17.40	$144 \times 144 \times 144$	1	2.83	661.1	198.3	1.39×10^5	0.8037	0.0057	0.0085
3×10^{-7}	21.74	$96 \times 96 \times 192$	0.5	4.24	1.00×10^3	300.5	1.7×10^5	0.5651	0.0059	0.0089
3×10^{-7}	30.44	$96 \times 96 \times 216$	0.2	9.59	2.28×10^3	683.9	8.3×10^4	0.0495	0.0065	0.0084
3×10^{-7}	43.49	$192 \times 192 \times 288$	0.06	17.67	3.94×10^3	1.18×10^3	3.6×10^5	0.0274	0.0069	0.0070
3×10^{-7}	60.89	$216 \times 216 \times 480$	0.005	27.87	4.37×10^3	1.31×10^3	9.5×10^5	0.0357	0.0054	0.0064
3×10^{-7}	78.28	$288 \times 288 \times 576$	0.003	41.72	5.05×10^3	1.51×10^3	1.5×10^6	0.0320	0.0048	0.0058
1×10^{-7}	11.31	$96 \times 96 \times 240$	4	1.53	402.1	120.6	2.0×10^5	0.9520	0.0037	0.0073
1×10^{-7}	14.78	$96 \times 96 \times 240$	4	2.19	703.3	211.0	2.6×10^5	0.9009	0.0039	0.0059
1×10^{-7}	17.39	$96 \times 96 \times 240$	3	2.83	954.9	286.5	2.6×10^5	0.8142	0.0039	0.0058
1×10^{-7}	21.74	$96 \times 96 \times 240$	1	4.21	1.45×10^3	434.3	3.1×10^5	0.5633	0.0041	0.0062
1×10^{-7}	26.09	$96 \times 96 \times 240$	0.5	6.23	2.07×10^3	620.2	4.0×10^5	0.3330	0.0041	0.0063
1×10^{-7}	30.44	$96 \times 96 \times 288$	0.2	8.85	2.75×10^3	825.5	5.5×10^5	0.1838	0.0042	0.0061
1×10^{-7}	43.48	$192 \times 192 \times 432$	0.05	16.08	4.51×10^3	1.35×10^3	1.3×10^6	0.0786	0.0040	0.0053
1×10^{-7}	60.88	$216 \times 216 \times 540$	0.02	26.50	5.85×10^3	1.75×10^3	2.3×10^6	0.0423	0.0036	0.0045
1×10^{-7}	78.27	$288 \times 288 \times 648$	0.01	37.55	7.25×10^3	2.17×10^3	2.58×10^6	0.0290	0.0035	0.0041

Table 3. Details of the numerical simulations for $Pm = 0.3$, $E = (1 \times 10^{-6}, 3 \times 10^{-7}, 1 \times 10^{-7})$ cases.

https://doi.org/10.1017/jfm.2022.848 Published online by Cambridge University Press

Pm	E	$\widetilde{Ra}$	$N_x \times N_y \times N_z$	Δt	Nu	Re	Rm	E_{mag}	$\bar{E}_{mag}/E_{mag}$	λ_u	λ_B
0.2	3×10^{-8}	11.31	$96 \times 96 \times 288$	20	1.56	603.4	120.7	4.8×10^5	0.9795	0.0024	0.0040
0.2	3×10^{-8}	14.78	$96 \times 96 \times 288$	4	2.32	1.11×10^3	222.0	8.9×10^5	0.9486	0.0026	0.0042
0.2	3×10^{-8}	17.39	$96 \times 96 \times 288$	4	2.95	1.47×10^3	294.1	8.3×10^5	0.9029	0.0026	0.0041
0.2	3×10^{-8}	21.74	$96 \times 96 \times 384$	2	4.27	2.18×10^3	435.0	7.90×10^5	0.7349	0.0027	0.0043
0.2	3×10^{-8}	30.44	$96 \times 96 \times 384$	0.6	8.48	4.02×10^3	803.3	1.1×10^6	0.3238	0.0028	0.0045
0.2	3×10^{-8}	43.48	$216 \times 216 \times 480$	0.06	15.77	7.02×10^3	1.40×10^3	2.8×10^6	0.1114	0.0028	0.0041
0.2	3×10^{-8}	60.87	$192 \times 192 \times 576$	0.01	23.80	9.37×10^3	1.87×10^3	4.0×10^6	0.0665	0.0026	0.0034
0.2	3×10^{-8}	78.27	$288 \times 288 \times 768$	0.005	36.44	1.11×10^4	2.22×10^3	7.9×10^6	0.0355	0.0023	0.0033
0.1	1×10^{-8}	11.30	$96 \times 96 \times 288$	5	1.574	926.1	92.6	—	—	0.0015	—
0.1	1×10^{-8}	14.78	$96 \times 96 \times 384$	5	2.48	1.67×10^3	167.0	2.9×10^6	0.9781	0.0018	0.0029
0.1	1×10^{-8}	17.39	$96 \times 96 \times 384$	5	3.16	2.24×10^3	223.8	3.5×10^6	0.9648	0.0018	0.0030
0.1	1×10^{-8}	21.74	$96 \times 96 \times 384$	2.5	4.47	3.22×10^3	322.0	3.1×10^6	0.9114	0.0019	0.0030
0.1	1×10^{-8}	30.44	$192 \times 192 \times 540$	0.5	8.08	5.43×10^3	543.4	3.3×10^6	0.6953	0.0019	0.0033
0.1	1×10^{-8}	43.48	$192 \times 192 \times 540$	0.15	16.63	1.02×10^4	1.02×10^3	6.2×10^6	0.3206	0.0019	0.0034
0.1	1×10^{-8}	60.87	$216 \times 216 \times 540$	0.04	24.34	1.28×10^4	1.28×10^3	8.7×10^6	0.2111	0.0017	0.0031
0.1	1×10^{-8}	78.26	$288 \times 288 \times 768$	0.04	33.73	1.46×10^4	1.46×10^3	1.0×10^7	0.1821	0.0016	0.0029
0.05	1×10^{-8}	14.78	$96 \times 96 \times 384$	6	2.40	1.76×10^3	87.8 ± 5.4	—	—	0.0018	—
0.05	1×10^{-8}	17.39	$96 \times 96 \times 540$	5	3.19	2.52×10^3	125.7	—	—	0.0019	—
0.05	1×10^{-8}	21.74	$96 \times 96 \times 540$	2	4.73	3.96×10^3	197.9	—	—	0.0020	—
0.05	1×10^{-8}	30.44	$96 \times 96 \times 540$	1	8.72	5.69×10^3	284.6	5.4×10^6	0.8772	0.0019	0.0034
0.05	1×10^{-8}	43.48	$216 \times 216 \times 576$	0.1	16.63	1.08×10^4	537.9	7.4×10^6	0.5926	0.0019	0.0036
0.05	1×10^{-8}	60.87	$216 \times 216 \times 648$	0.015	23.38	1.31×10^4	653.4	9.0×10^6	0.4477	0.0017	0.0036
0.05	1×10^{-8}	78.26	$288 \times 288 \times 864$	0.01	32.17	1.53×10^4	765.1	1.1×10^7	0.3665	0.0016	0.0035

Table 4. Details of the numerical simulations for $Pm = 0.2$, $E = 3 \times 10^{-8}$ cases, $Pm = 0.1$, $E = 1 \times 10^{-8}$ cases and $Pm = 0.05$, $E = 1 \times 10^{-8}$ cases.

References

Aubert, J. 2005 Steady zonal flows in spherical shell dynamos. *J. Fluid Mech.* **542**, 53–67.

Aubert, J., Gastine, T. & Fournier, A. 2017 Spherical convective dynamos in the rapidly rotating asymptotic regime. *J. Fluid Mech.* **813**, 558–593.

Aurnou, J.M., Bertin, V., Grannan, A.M., Horn, S. & Vogt, T. 2018 Rotating thermal convection in liquid gallium: multi-modal flow, absent steady columns. *J. Fluid Mech.* **846**, 846–876.

Aurnou, J.M., Calkins, M.A., Cheng, J.S., Julien, K., King, E.M., Nieves, D., Soderlund, K.M. & Stellmach, S. 2015 Rotating convective turbulence in Earth and planetary cores. *Phys. Earth Planet. Inter.* **246**, 52–71.

Bushby, P.J., Käpylä, P.J., Masada, Y., Brandenburg, A., Favier, B., Guervilly, C. & Käpylä, M.J. 2018 Large-scale dynamos in rapidly rotating plane layer convection. *Astron. Astrophys.* **612**, A97.

Calkins, M.A. 2018 Quasi-geostrophic dynamo theory. *Phys. Earth Planet. Inter.* **276**, 182–189.

Calkins, M.A., Julien, K. & Tobias, S.M. 2017 Inertia-less convectively-driven dynamo models in the limit of low Rossby number. *Phys. Earth Planet. Inter.* **266**, 54–59.

Calkins, M.A., Julien, K., Tobias, S.M. & Aurnou, J.M. 2015 A multiscale dynamo model driven by quasi-geostrophic convection. *J. Fluid Mech.* **780**, 143–166.

Calkins, M.A., Long, L., Nieves, D., Julien, K. & Tobias, S.M. 2016 Convection-driven kinematic dynamos at low Rossby and magnetic Prandtl numbers. *Phys. Rev. Fluids* **1**, 083701.

Calkins, M.A., Orvedahl, R.J. & Featherstone, N.A. 2021 Large-scale balances and asymptotic scaling behaviour in spherical dynamos. *Geophys. J. Intl* **227** (2), 1228–1245.

Cattaneo, F. & Hughes, D.W. 1996 Nonlinear saturation of the turbulent α effect. *Phys. Rev.* E **54** (5), R4532.

Cattaneo, F. & Hughes, D.W. 2006 Dynamo action in a rotating convective layer. *J. Fluid Mech.* **553**, 401–418.

Cattaneo, F. & Hughes, D.W. 2017 Dynamo action in rapidly rotating Rayleigh–Bénard convection at infinite Prandtl number. *J. Fluid Mech.* **825**, 385–411.

Chandrasekhar, S. 1961 *Hydrodynamic and Hydromagnetic Stability*. Oxford University Press.

Cheng, J.S., Stellmach, S., Ribeiro, A., Grannan, A., King, E.M. & Aurnou, J.M. 2015 Laboratory-numerical models of rapidly rotating convection in planetary cores. *Geophys. J. Intl* **201**, 1–17.

Childress, S. & Soward, A.M. 1972 Convection-driven hydromagnetic dynamo. *Phys. Rev. Lett.* **29** (13), 837–839.

Christensen, U. & Aubert, J. 2006 Scaling properties of convection-driven dynamos in rotating shells and applications to planetary magnetic fields. *Geophys. J. Intl* **166**, 97–114.

Dormy, E. 2016 Strong-field spherical dynamos. *J. Fluid Mech.* **789**, 500–513.

Dormy, E., Soward, A.M., Jones, C.A., Jault, D. & Cardin, P. 2004 The onset of thermal convection in rotating spherical shells. *J. Fluid Mech.* **501**, 43–70.

Fautrelle, Y. & Childress, S. 1982 Convective dynamos with intermediate and strong fields. *Geophys. Astrophys. Fluid Dyn.* **22** (3), 235–279.

Favier, B. & Bushby, P.J. 2013 On the problem of large-scale magnetic field generation in rotating compressible convection. *J. Fluid Mech.* **723**, 529–555.

Favier, B., Silvers, L.J. & Proctor, M.R.E. 2014 Inverse cascade and symmetry breaking in rapidly rotating Boussinesq convection. *Phys. Fluids* **26**, 096605.

Golitsyn, G.S. 1960 Fluctuations of the magnetic field and current density in a turbulent flow of a weakly conducting fluid. In *Soviet Physics Doklady*, vol. 5, p. 536.

Guervilly, C., Hughes, D.W. & Jones, C.A. 2014 Large-scale vortices in rapidly rotating Rayleigh–Bénard convection. *J. Fluid Mech.* **758**, 407–435.

Guervilly, C., Hughes, D.W. & Jones, C.A. 2017 Large-scale-vortex dynamos in planar rotating convection. *J. Fluid Mech.* **815**, 333–360.

Guzmán, A.J.A., Madonia, M., Cheng, J.S., Ostilla-Mónico, R., Clercx, H.J.H. & Kunnen, R.P.J. 2021 Force balance in rapidly rotating Rayleigh–Bénard convection. *J. Fluid Mech.* **928**, A16.

Hughes, D.W. & Cattaneo, F. 2016 Strong-field dynamo action in rapidly rotating convection with no inertia. *Phys. Rev.* E **93**, 061101R.

Hughes, D.W. & Cattaneo, F. 2019 Force balance in convectively driven dynamos with no inertia. *J. Fluid Mech.* **879**, 793–807.

Jones, C.A. 2011 Planetary magnetic fields and fluid dynamos. *Annu. Rev. Fluid Mech.* **43**, 583–614.

Jones, C.A. 2015 Thermal and compositional convection in the outer core. In *Treatise on Geophysics* (ed. G. Schubert), vol. 8, pp. 115–159. Elsevier.

Jones, C.A. & Roberts, P.H. 2000 Convection-driven dynamos in a rotating plane layer. *J. Fluid Mech.* **404**, 311–343.

JULIEN, K., KNOBLOCH, E. & WERNE, J. 1998 A new class of equations for rotationally constrained flows. *Theor. Comput. Fluid Dyn.* **11**, 251–261.

JULIEN, K., RUBIO, A.M., GROOMS, I. & KNOBLOCH, E. 2012 Statistical and physical balances in low Rossby number Rayleigh–Bénard convection. *Geophys. Astrophys. Fluid Dyn.* **106** (4–5), 392–428.

KÄPYLÄ, P.J., KORPI, M.J. & BRANDENBURG, A. 2009 Large-scale dynamos in rigidly rotating turbulent convection. *Astrophys. J.* **697**, 1153–1163.

KOLHEY, P., STELLMACH, S. & HEYNER, D. 2022 Influence of boundary conditions on rapidly rotating convection and its dynamo action in a plane fluid layer. *Phys. Rev. Fluids* **7** (4), 043502.

KUTZNER, C. & CHRISTENSEN, U.R. 2002 From stable dipolar towards reversing numerical dynamos. *Phys. Earth Planet. Inter.* **131**, 29–45.

LI, S., JAROSZYNSKI, S., PEARSE, S., ORF, L. & CLYNE, J. 2019 VAPOR: a visualization package tailored to analyze simulation data in earth system science. *Atmosphere* **10** (9), 488.

MADONIA, M., GUZMÁN, A.J.A., CLERCX, H.J.H. & KUNNEN, R.P.J. 2021 Velocimetry in rapidly rotating convection: spatial correlations, flow structures and length scales (a). *Europhys. Lett.* **135** (5), 54002.

MAFFEI, S., CALKINS, M.A., JULIEN, K. & MARTI, P. 2019 Magnetic quenching of the inverse cascade in rapidly rotating convective turbulence. *Phys. Rev. Fluids* **4** (4), 041801.

MAFFEI, S., KROUSS, M.J., JULIEN, K. & CALKINS, M.A. 2021 On the inverse cascade and flow speed scaling behaviour in rapidly rotating Rayleigh–Bénard convection. *J. Fluid Mech.* **913**, A18.

MALKUS, W.V.R. & PROCTOR, M.R.E. 1975 The macrodynamics of α-effect dynamos in rotating fluids. *J. Fluid Mech.* **67**, 417–443.

MARTI, P., CALKINS, M.A. & JULIEN, K. 2016 A computationally efficient spectral method for modeling core dynamics. *Geochem. Geophys. Geosyst.* **17** (8), 3031–3053.

MOFFATT, K. & DORMY, E. 2019 *Self-Exciting Fluid Dynamos*, vol. 59. Cambridge University Press.

ORVEDAHL, R.J., FEATHERSTONE, N.A. & CALKINS, M.A. 2021 Large-scale magnetic field saturation and the Elsasser number in rotating spherical dynamo models. *Mon. Not. R. Astron. Soc.* **507** (1), L67–L71.

OSSENDRIJVER, M. 2003 The solar dynamo. *Astron. Astrophys. Rev.* **11** (4), 287–367.

PARKER, E.N. 1955 Hydromagnetic dynamo models. *Astrophys. J.* **122**, 293–314.

PLUMLEY, M., JULIEN, K., MARTI, P. & STELLMACH, S. 2016 The effects of Ekman pumping on quasi-geostrophic Rayleigh–Bénard convection. *J. Fluid Mech.* **803**, 51–71.

POPE, S.B. 2000 *Turbulent Flows*. Cambridge University Press.

ROBERTS, P.H. 1988 Future of geodynamo theory. *Geophys. Astrophys. Fluid Dyn.* **44**, 3–31.

ROBERTS, P.H. & KING, E.M. 2013 On the genesis of the Earth's magnetism. *Rep. Prog. Phys.* **76**, 096801.

ROBERTS, P.H. & ZHANG, K. 2000 Thermal generation of Alfvén waves in oscillatory magnetoconvection. *J. Fluid Mech.* **420**, 201–223.

RUBIO, A.M., JULIEN, K., KNOBLOCH, E. & WEISS, J.B. 2014 Upscale energy transfer in three-dimensional rapidly rotating turbulent convection. *Phys. Rev. Lett.* **112**, 144501.

SCHAEFFER, N., JAULT, D., NATAF, H.-C. & FOURNIER, A. 2017 Turbulent geodynamo simulations: a leap towards Earth's core. *Geophys. J. Intl* **211** (1), 1–29.

SCHEKOCHIHIN, A.A., ISKAKOV, A.B., COWLEY, S.C., MCWILLIAMS, J.C., PROCTOR, M.R.E. & YOUSEF, T.A. 2007 Fluctuation dynamo and turbulent induction at low magnetic Prandtl numbers. *New J. Phys.* **9** (8), 300.

SCHUBERT, G. & SODERLUND, K. 2011 Planetary magnetic fields: observations and models. *Phys. Earth Planet. Inter.* **187**, 92–108.

SCHWAIGER, T., GASTINE, T. & AUBERT, J. 2021 Relating force balances and flow length scales in geodynamo simulations. *Geophys. J. Intl* **224** (3), 1890–1904.

SHEYKO, A., FINLAY, C., FAVRE, J. & JACKSON, A. 2018 Scale separated low viscosity dynamos and dissipation within the Earth's core. *Sci. Rep.* **8** (1), 12566.

SODERLUND, K.M., KING, E.M. & AURNOU, J.M. 2012 The influence of magnetic fields in planetary dynamo models. *Earth Planet. Sci. Lett.* **333–334**, 9–20.

SOWARD, A.M. 1974 A convection-driven dynamo: I. The weak field case. *Phil. Trans. R. Soc. Lond.* A **275**, 611–646.

SPALART, P.R., MOSER, R.D. & ROGERS, M.M. 1991 Spectral methods for the Navier–Stokes equations with one infinite and two periodic directions. *J. Comput. Phys.* **96**, 297–324.

SPRAGUE, M., JULIEN, K., KNOBLOCH, E. & WERNE, J. 2006 Numerical simulation of an asymptotically reduced system for rotationally constrained convection. *J. Fluid Mech.* **551**, 141–174.

STEENBECK, M., KRAUSE, F. & RÄDLER, K.-H. 1966 A calculation of the mean electromotive force in an electrically conducting fluid in turbulent motion, under the influence of Coriolis forces. *Z. Naturforsch.* **21a**, 369–376.

STELLMACH, S. & HANSEN, U. 2004 Cartesian convection driven dynamos at low Ekman number. *Phys. Rev.* E **70**, 056312.

STELLMACH, S., LISCHPER, M., JULIEN, K., VASIL, G., CHENG, J.S., RIBEIRO, A., KING, E.M. & AURNOU, J.M. 2014 Approaching the asymptotic regime of rapidly rotating convection: boundary layers versus interior dynamics. *Phys. Rev. Lett.* **113**, 254501.

TILGNER, A. 2012 Transitions in rapidly rotating convection driven dynamos. *Phys. Rev. Lett.* **109**, 248501.

TILGNER, A. 2014 Magnetic energy dissipation and mean magnetic field generation in planar convection-driven dynamos. *Phys. Rev.* E **90**, 013004.

TOBIAS, S.M. 2021 The turbulent dynamo. *J. Fluid Mech.* **912**, P1.

VAINSHTEIN, S.I. & CATTANEO, F. 1992 Nonlinear restrictions on dynamo action. *Astrophys. J.* **393**, 165–171.

VOGT, T., HORN, S. & AURNOU, J.M. 2021 Oscillatory thermal–inertial flows in liquid metal rotating convection. *J. Fluid Mech.* **911**, A5.

YADAV, R.K., GASTINE, T. & CHRISTENSEN, U.R. 2016 Approaching a realistic force balance in geodynamo simulations. *Proc. Natl Acad. Sci. USA* **113** (43), 12065–12070.

YAN, M. & CALKINS, M.A. 2022 Strong large scale magnetic fields in rotating convection-driven dynamos: the important role of magnetic diffusion. *Phys. Rev. Res.* **4** (1), L012026.

YAN, M., CALKINS, M.A., MAFFEI, S., JULIEN, K., TOBIAS, S.M. & MARTI, P. 2019 Heat transfer and flow regimes in quasi-static magnetoconvection with a vertical magnetic field. *J. Fluid Mech.* **877**, 1186–1206.

YAN, M., TOBIAS, S.M. & CALKINS, M.A. 2021 Scaling behaviour of small-scale dynamos driven by Rayleigh–Bénard convection. *J. Fluid Mech.* **915**, A15.